Real-time prediction of alongshore near-field tsunami runup distribution from heterogeneous earthquake slip distribution

Jun-Whan Lee[1], Jennifer L. Irish[1,2], Robert Weiss[1,3]

[1]Center for Coastal Studies, Virginia Tech, 926 W Campus Dr, Blacksburg, VA 24061, USA
[2]Department of Civil and Environmental Engineering, Virginia Tech, 750 Drillfield Dr, Blacksburg, VA, 24061, USA
[3]Department of Geosciences, Virginia Tech, 926 W Campus Dr, Blacksburg, VA, 24061, USA

Key Points:

- A rapid data-driven model is proposed that can predict tsunami runup distribution from heterogeneous earthquake slip distribution.
- The data-driven model is validated based on synthetic tsunami scenarios and the 2011 Tohoku tsunami.
- This model has potential for supporting real-time tsunami forecasting.

Corresponding author: Jun-Whan Lee, `jwlee89@vt.edu`

Abstract

Real-time tsunami prediction is necessary for tsunami forecasting. Although tsunami forecasting based on a pre-computed tsunami simulation database is fast, it is difficult to respond to earthquakes that are not in the database. As the computation speed increases, various alternatives based on physics-based models have been proposed. However, physics-based models still require several minutes to simulate tsunamis and can have numerical stability issues that potentially make them unreliable for use in forecasting–particularly in the case of near-field tsunamis. This paper presents a data-driven model called the tsunami runup response function for finite faults (TRRF-FF) model that can predict alongshore near-field tsunami runup distribution from heterogeneous earthquake slip distribution in less than a second. Once the TRRF-FF model is trained and calibrated based on a discrete set of tsunami simulations, the TRRF-FF model can predict alongshore tsunami runup distribution from any combination of finite fault parameters. The TRRF-FF model treats the leading order contribution and the residual part of the alongshore tsunami runup distribution separately. The interaction between finite faults is modeled based on the leading order alongshore tsunami runup distribution. We validated the TRRF-FF modeling approach with more than 200 synthetic tsunami scenarios in eastern Japan. We further explored the performance of the TRRF-FF model by applying it to the 2011 Tohoku (Japan) tsunami event. The results show that the TRRF-FF model is more flexible, occupies much less storage space than a pre-computed tsunami simulation database, and is more rapid and reliable than real-time physics-based numerical simulation.

Plain Language Summary

Timely tsunami warning is important to save lives and property. Existing physics-based models require a lot of time to predict tsunamis. For this reason, many countries rely on a pre-computed tsunami simulation database for tsunami warning. However, such databases do not include all possible tsunami scenarios, because in the real world there is almost an infinite number of possible tsunamigenic-earthquakes. The present study introduces a new data-driven model that can rapidly predict the maximum onshore tsunami height along the coast from the earthquake information. Once the model is trained based on physics-based model simulations, the new model can be applied to any possible tsunami scenario. This new model captures the leading order contribution and the residual part of the alongshore tsunami runup distribution separately. This new model can account for complex large earthquakes with different land movements depending on location. We tested this new model using artificial earthquake scenarios as well as the historic Japan earthquake from 2011. The results show that the new model can handle wider variety of scenarios than the traditional database approach, and the new model takes up less storage space. Moreover, the new model is more rapid and reliable than a physics-based model.

1 Introduction

Timely tsunami forecasting and dissemination of warnings are challenging tasks, especially for near-field tsunamis, which can arrive onshore in a few minutes (National Research Council, 2011). For example, the 1960 Chile tsunami (M_W9.5) arrived on Chilean coasts about 15-20 minutes after the earthquake, and the earthquake and the subsequent tsunami took 1,655 lives (Igarashi et al., 2011). The 2011 Tohoku (Japan) tsunami (M_W9.0) also hit the Japanese mainland 20 minutes after the earthquake, killing 15,641 people (Mori et al., 2011). Given that the evacuation starting time is one of the key factors related to fatality rates (Yun & Hamada, 2015), it is critical to minimize the time required for tsunami forecasting.

The tsunami forecasting process usually consists of two steps. The first step is a tsunami source inversion to determine tsunami source characteristics (e.g., earthquake fault parameters) from recorded waveforms once the earthquake is detected. Over the

last several decades, there have been several efforts to improve the accuracy and reduce the computational time of the inversion models based on various types of sensors such as broadband seismometers, strong-motion accelerometers, tide gauges, GNSS (Global Navigation Satellite System) sensors, InSAR (Interferometric Synthetic Aperture Radar), and ocean-bottom pressure gauges (e.g., Blewitt et al., 2006, 2009; Maeda et al., 2015; Melgar & Bock, 2013; Ohta et al., 2012; Wei et al., 2014; Xie & Meng, 2020; Yokota et al., 2011; Yoshimoto et al., 2016). Instead of inferring earthquake information, some studies suggest methods to directly estimate the tsunami's initial free-surface displacement from the observations without any assumptions about the earthquake (Saito et al., 2010; Tsushima et al., 2009, 2011, 2012, 2014). Recent progress in the first step of tsunami forecasting can be found in Tsushima and Ohta (2014) and Y. Wang, Tsushima, et al. (2021).

The second step of tsunami forecasting is tsunami forward modeling to estimate a tsunami impact from the inferred tsunami source. And this study will focus on reducing the computation time of the tsunami forward modeling, which is important for minimizing the tsunami forecasting time once the tsunami source is identified. As powerful parallel computers become available, some studies suggested a direct high-fidelity physics-based numerical simulation for tsunami forward modeling (e.g., Inoue et al., 2019; Løvholt et al., 2019; Melgar et al., 2016; Musa et al., 2018; Oishi et al., 2015). The problem, however, is that not all countries can afford powerful computers. Moreover, the high-fidelity physics-based numerical simulation may have a stability issue depending on the numerical scheme, grids, and time step. Such instabilities can prevent the timely and/or accurate real-time forecasting that is critical when lives and property are at stake. For this reason, most of the forward modeling for tsunami forecasting still relies on a pre-computed tsunami simulation database that can provide rapid and stable estimates by looking up the most closely related event from the database as soon as tsunami source information becomes available (e.g., Greenslade et al., 2011; Hoshiba & Ozaki, 2014; Kamigaichi, 2022; Lauterjung et al., 2014; Selva et al., 2021) and/or using the physics-based model as a backup to handle tsunami events outside the database coverage (e.g., Harig et al., 2020). Although the pre-computed tsunami simulation database approach is rapid, this approach may result in a significant error if the actual tsunami is not represented in the database. Moreover, most existing databases provide the maximum tsunami height at the shoreline as an output, which does not fully illustrate the tsunami inundation process (Gusman et al., 2014).

To provide tsunami inundation predictions, some studies suggested a method that combines rapid low-fidelity, physics-based models, pre-computed databases (e.g., Gusman et al., 2014; Gusman & Tanioka, 2015; Mulia et al., 2018; Setiyono et al., 2017; Tanioka et al., 2014, 2020), and machine learning techniques (e.g., Fauzi & Mizutani, 2020; Mulia et al., 2020) in tsunami forward modeling. These approaches are much faster than a direct high-fidelity, physics-based numerical simulation. However, the low-fidelity, physics-based model (e.g., solving linear shallow water wave equations) still requires several minutes to execute and can have numerical stability issues. These limitations may prevent or hinder timely and effective evacuation from near-field tsunamis. Recently, Mulia et al. (2022) proposed a machine-learning model that can rapidly estimate tsunami inundation directly from 150 offshore observations to overcome the computational burden of physics-based models. However, Mulia et al.'s proposed machine learning approach can be applied only to a limited area, such as East Japan, where there are enough offshore observation stations.

A Tsunami Runup Response Function (TRRF) model is a data driven model that can rapidly predict a distribution of tsunami runup along the coast (hereafter alongshore tsunami runup distribution) from earthquake fault parameters (J.-W. Lee et al., 2020). The basic concept of the TRRF model is to decompose the alongshore tsunami runup distribution into a leading-order contribution that can be modeled by fault parameters using the Okal and Synolakis (2004)'s empirical formula and the residual part

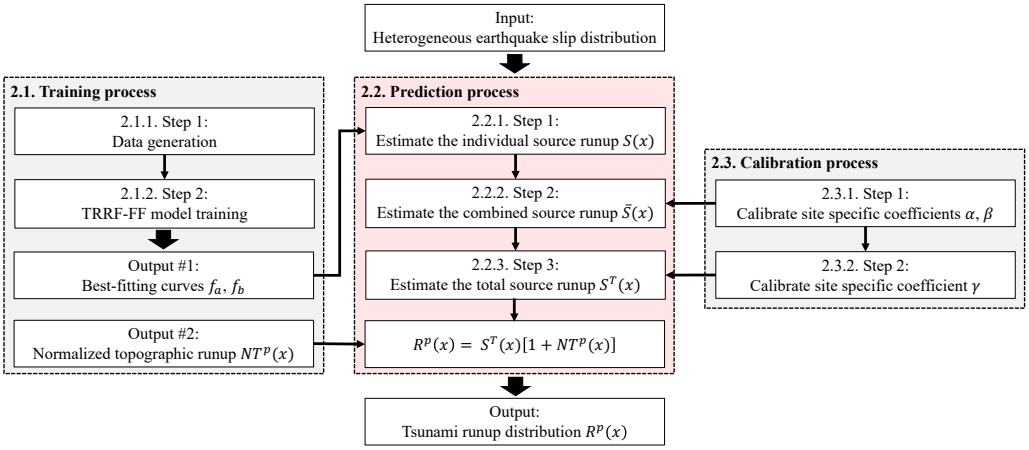

Figure 1. Flow chart of TRRF-FF model. The training process and the calibration process are required only once to proceed with the prediction process.

that captures the influence of local topography. Although the TRRF model may be faster than most of the methods mentioned above, there is a limitation that the TRRF model can be applied only to a uniform slip earthquake source. This limitation can be critical for tsunami forecasting, especially for tsunamis caused by earthquakes with $M_W \geq 8.0$, given that the alongshore tsunami runup distribution can vary depending on the heterogeneity of earthquake slip distribution even when the earthquake magnitude is the same (Geist, 2002; LeVeque et al., 2016; Li et al., 2016; Mueller et al., 2015; Ulutas, 2013).

This study proposes a new data-driven model that can rapidly predict the spatial distribution of tsunami runups along the coastline from the heterogeneous earthquake slip distribution. Hereafter we referred to this model as the TRRF-FF model, which stands for Tsunami Runup Response Function applicable to the Finite Faults model. The TRRF-FF model can consider the heterogeneous earthquake slip distribution by modeling the interaction between finite faults based on the leading order contribution of alongshore tsunami runup distribution (Section 2). We investigate the performance of the TRRF-FF model based on synthetic tsunami events (Section 3) and the 2011 Tohoku tsunami (Section 4). Then, we discuss the characteristics of the TRRF-FF model and future work (Section 5). A summary of this study is provided in Section 6.

2 Tsunami Runup Response Function applicable to Finite Faults (TRRF-FF) Model

Figure 1 shows the flow chart of the TRRF-FF model, which is divided into three processes: training process (Section 2.1), prediction process (Section 2.2), and calibration process (Section 2.3). Once the TRRF-FF model is trained and calibrated based on a discrete set of physics-based simulations (see gray dashed boxes in Figure 1), the alongshore tsunami runup distribution can be estimated in less than a second from heterogeneous earthquake slip distribution (see red dashed boxes in Figure 1).

2.1 Training process

The TRRF-FF model can be trained based on a discrete set of physics-based simulations. Here, we summarize the training process in two steps: (1) data generation and (2) TRRF-FF model training (see Figure 1).

ID	LON (°E)	LAT (°N)	STR (°)
24a	142.9795	40.349	185
24b	143.5273	40.3125	185
24z	142.4312	40.3856	185
25a	142.8839	39.4541	185
25b	143.4246	39.4176	185
25z	142.3426	39.4907	185
26a	142.7622	38.5837	188
26b	143.293	38.5254	188
26z	142.2308	38.6421	188
27a	142.532	37.783	198
27b	143.0357	37.6534	198
27z	142.0269	37.9126	198
28a	142.1315	37.0265	208
28b	142.5941	36.8297	208
28z	141.6671	37.2234	208

Table 1. Center position and strike angle of unit source. The ID of the unit sources corresponds to Figure 2. LON is longitude, LAT is latitude, and STR is strike angle.

Fault parameter	Low	Central	High
DIP (°)	10	20	30
SLP (m)	4	16	28
DEP (km)	5	30	55
LEN (km)		100	
WID (km)		50	
RAK (°)		90	

Table 2. Three-level (low, central, and high) fault parameters used for TRRF-FF model training. DIP is dip angle, SLP is slip, DEP is top-edge depth, LEN is fault length, WID is fault width, and RAK is rake angle.

2.1.1 Step 1: Data generation

In this study, we chose East Japan and defined 15 tsunami unit sources (hereafter finite faults) along the Japan trench following the pre-defined tsunami unit sources of the National Oceanic and Atmospheric Administration's Center for Tsunami Research (NCTR), which are being used for tsunami forecasting in the United States (see black rectangles in Figure 2). Each finite fault has a fault length of 100 km, a fault width of 50 km, and a rake of 90°. The center position and strike angle of each finite fault can be found in Table 1. For each finite fault, 27 ($= 3^3$) tsunamigenic-earthquake scenarios were generated by considering three levels of dip angle, slip, and top-edge depth (Table 2); in all, 405 ($= 15{\cdot}27$) unique scenarios are considered. The range of the dip angle and the top-edge depth was defined based on the characteristics of subduction-interface earthquakes (Thingbaijam et al., 2017). The range of slip was set to 4 m−28 m in order to cover the slip range of Tang et al. (2012)'s tsunami source. Note that we assumed 15 tsunami unit sources in this study to demonstrate the TRRF-FF modeling framework. It will be necessary to consider more tsunami unit sources, covering a wider subduction zone, to respond to possible future tsunamis.

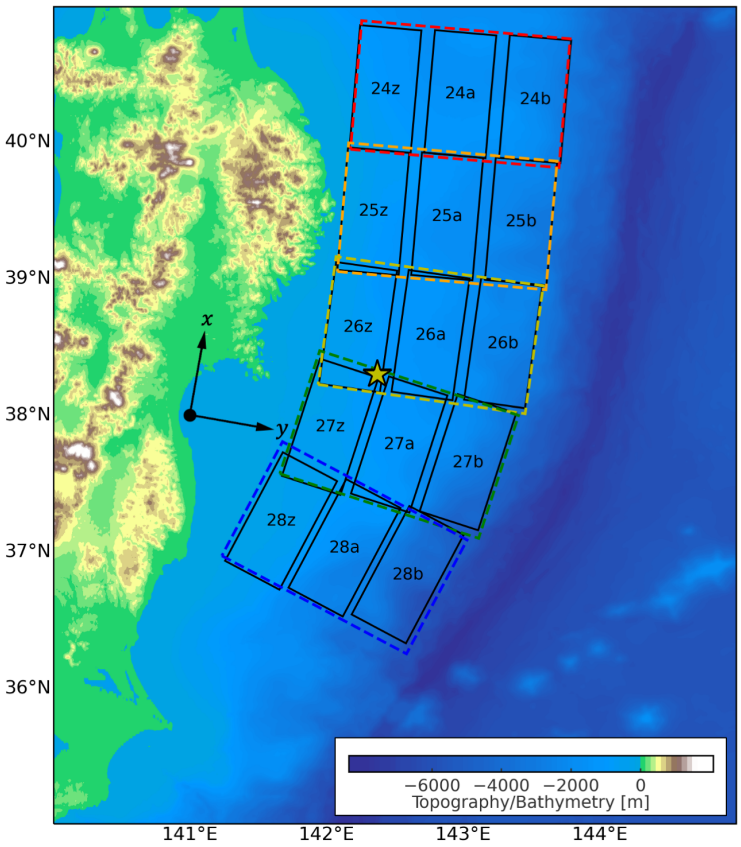

Figure 2. Map of East Japan. Black rectangles represent the pre-defined tsunami unit sources of the National Oceanic and Atmospheric Administration's Center for Tsunami Research (NCTR)'s database (Gica, 2015). The numbering of the unit sources corresponds to Gica (2015). Each unit source has a fault length of 100 km, a fault width of 50 km, and a rake of 90°. The dashed rectangles represent the unit sources grouped to build the TRRF-FF model. The black circle is the origin used to convert the location information from a spherical coordinate system to a Cartesian coordinate system. The yellow star is the USGS epicenter for the 2011 Tohoku earthquake.

We simulated all 405 tsunamigenic-earthquake scenarios using the numerical model Basilisk, which solves the Green–Naghdi equations with an Adaptive Mesh Refinement (AMR) technique (Popinet, 2015). The initial tsunami free surface displacement was estimated from earthquake fault parameters using the Okada (1985) model for instantaneous fault rupture. We used a 15-arc-second bathymetry (GEBCO Compilation Group, 2019) and fixed the bottom drag coefficient of a quadratic drag law to 10^{-4}. The tsunami elapsed time was set to three hours which was long enough to capture the maximum runup. The maximum water level values were bilinearly interpolated onto a regular grid (0.004° intervals). Since the TRRF-FF model requires a Cartesian coordinate system, we converted the coordinate system from a spherical coordinate system to a Cartesian coordinate system using the Vincenty (1975)'s formula and a reference point ($38°N$, $141°E$) (see the black circle in Figure 2). We extracted the tsunami runup values along transects in the y-axis direction, at increments of 0.004°. Based on its average orientation, we assumed that the coastline (x-axis) is rotated 10 degrees clockwise from the north on average (see black arrow in Figure 2).

2.1.2 Step 2: TRRF-FF model training

We trained the TRRF-FF model based on 405 simulation results. For each simulation result, we decomposed the alongshore tsunami runup distribution $R(x)$ into source runup $S(x)$ and topographic runup $T(x)$ (Eq. 1).

$$R(x) = S(x) + T(x) \tag{1}$$

The source runup $S(x)$ is the best-fitting curve based on Okal and Synolakis (2004)'s empirical formula (Eq. 2).

$$S(x) = \frac{b}{\left[\frac{x-X}{a}\right]^2 + 1} \tag{2}$$

where the coefficient a is the width of the source runup, b is the maximum source runup, and X represents the center position of the finite fault in x direction, as defined in Figure 2. We used non-linear least squares to estimate the parameters of the empirical formula.

Then, we grouped the coefficients a and b estimated from the simulation scenarios that have the same unit source number (see dashed rectangles in Figure 2). For each group (81 scenarios per group), we fit the fault parameters and the corresponding coefficients a and b to a second-order polynomial model.

$$a = f_a(Y, DIP, SLP, DEP) \tag{3}$$

$$b = f_b(Y, DIP, SLP, DEP) \tag{4}$$

where f_a and f_b are best-fitting curves, Y is the center position of the finite fault in y direction, DIP is dip angle, SLP is slip, and DEP is top-edge depth. Note that the fault length and fault width are not included in Eqs. (3) and (4), unlike Eqs. (7) and (8) in J.-W. Lee et al. (2020), because the finite-fault size is fixed in this study. Figure 3 shows how the predicted coefficient values based on the second-order polynomial models (y-axis) fit well with the target coefficient values derived by fitting Eq. (2) to the 405 simulation results (x-axis).

The normalized topographic runup $NT(x)$, which represents the influence of the local topographic and bathymetric characteristics, was calculated for each simulation.

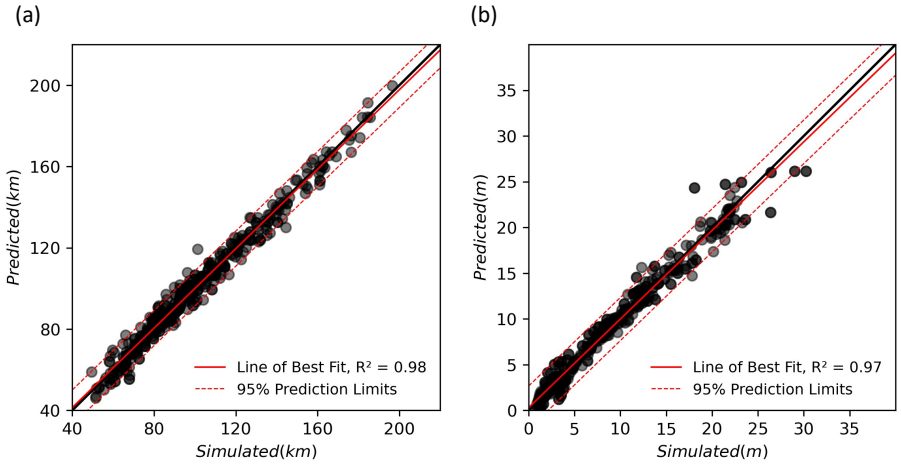

Figure 3. Comparison between the coefficient values derived by fitting Eq. 2 to the 405 simulation results (x-axis) and the predicted coefficient values based on the second-order polynomial models (Eqs. 3 and 4) (y-axis). Each gray circle represents (a) coefficient a and (b) coefficient b of Eq. 2.

$$NT(x) = \frac{T(x)}{S(x)} \tag{5}$$

Lastly, we extracted the median values ($NT^p(x)$) among 405 normalized topographic runups $NT(x)$, which will be used in the prediction process (see red line in Figure 4).

Once f_a and f_b (output #1 in Figure 1) and the normalized topographic runup for prediction $NT^p(x)$ (output #2 in Figure 1) are derived, the training process is finished and does not have to be repeated to proceed with the prediction process.

2.2 Prediction process

Once the TRRF-FF model is trained, the alongshore tsunami runup distribution $R^p(x)$ can be estimated using Eq. (6), which can be derived by combining Eq. (1) and Eq. (5).

$$R^p(x) = S^T(x)\,[1 + NT^p(x)] \tag{6}$$

where $NT^p(x)$ is the normalized topographic runup for the prediction that is derived in the training process, and $S^T(x)$ is a total source runup that can be estimated from heterogeneous earthquake slip distribution. Here, we demonstrate how to estimate the total source runup $S^T(x)$ in three steps.

2.2.1 Step 1: Estimate the individual source runup

For each finite fault where the slip is not equal to zero (hereafter activated finite fault), the source runup $S(x)$ is estimated using Eq. (2). The coefficients a and b in Eq. (2) are estimated using the Eqs. (3) and (4) that correspond to the finite fault location.

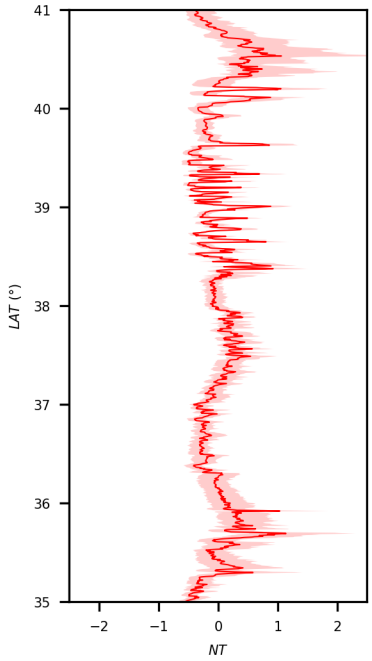

Figure 4. Normalized topographic runup for prediction $NT^p(x)$ of East Japan (Red line). The light red represents the range between 25th and 75th percentiles.

2.2.2 Step 2: Estimate the combined source runup

The second step is to combine source runups in the dip direction. This step is divided into three scenarios depending on the number of activated finite faults in the dip direction (Figure 5).

First, if there is only one activated finite fault in the dip direction (Figure 5a), the combined source runup $\bar{S}(x)^j$ is equal to the source runup of the activated finite fault calculated in step 1, where j is the unit source ID number.

Second, if there are two activated finite faults in the dip direction (Figure 5b), the combined source runup $\bar{S}(x)^j$ is not equal to the sum of the source runups of the activated finite faults. Due to the nonlinear interaction of tsunami waves caused by two finite faults, the combined source runup $\bar{S}(x)^j$ near the X (the center position of the finite fault in x direction) is smaller than the summation of individual source runups. The maximum value of the combined source runup is between the two individual source runups. In this study, we characterized the interaction of tsunami waves caused by two finite faults by introducing an interaction term $I(x)^{SLP}$.

$$\bar{S}(x)^j = S(x)_1^j + I(x)^{SLP} \cdot S(x)_2^j \tag{7}$$

where the $S(x)_1^j$ and $S(x)_2^j$ are the source runups – that are calculated in the first step. Note that subscript 1 refers to the activated finite fault that shows a relatively larger coefficient b value of Eq. (2) (see Figure 5b). To model a runup characteristic that becomes gradually smaller than the sum of the two source runups as it gets closer to X, the interaction term $I(x)^{SLP}$ is defined in a form similar to Okal and Synolakis (2004)'s empirical formula.

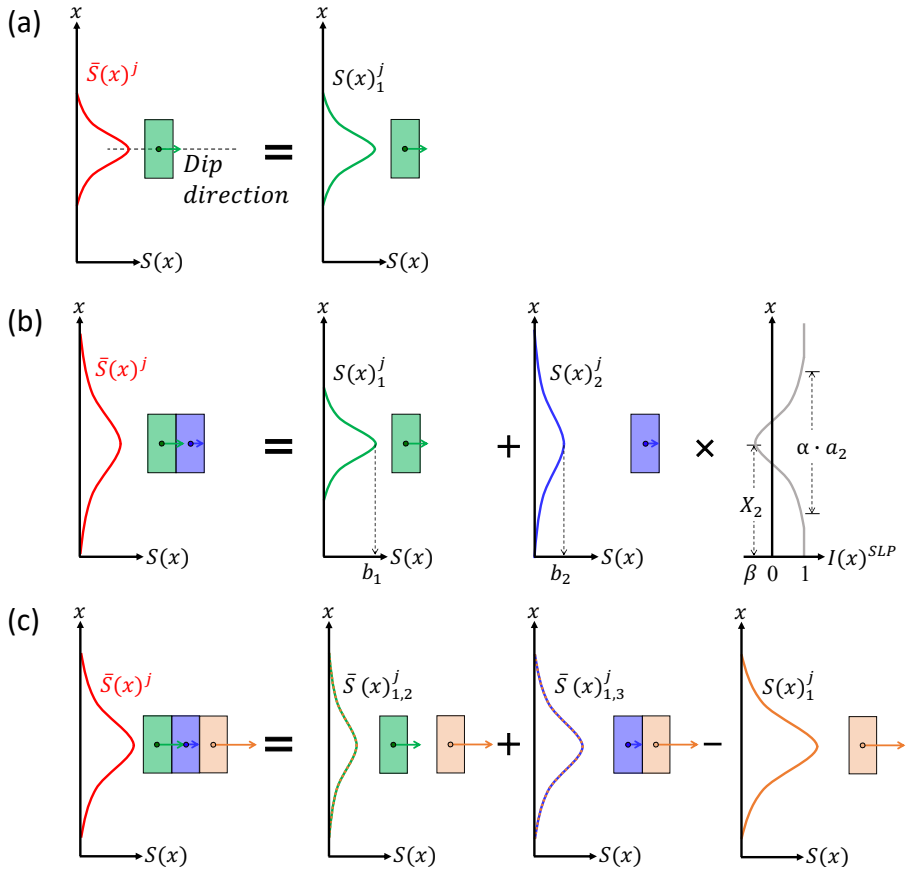

Figure 5. Schematic sketch of step 2 of the prediction process: (a) one, (b) two, or (c) three activated finite faults in the dip direction. The red line is a combined source runup $\bar{S}(x)^j$. The rectangles represent the activated finite faults. The gray line represents the interaction term $I(x)^{SLP}$.

$$I(x)^{SLP} = 1 - \frac{1+\beta}{\left[\frac{x-X_2}{\alpha \cdot a_2}\right]^2 + 1} \tag{8}$$

where X_2 and a_2 represent the center position of the finite fault in x direction and the coefficient a of the $S(x)_2^j$ in Eq. (2), respectively. The site-specific coefficients α and β are need to be calibrated in advance based on an extra set of physics-based simulations (see Section 2.3). Note that Eqs. (7) and (8) can also be applied to the case where the two activated finite faults are not adjacent to each other (For example, 24b and 24z in Figure 2).

Third, if there are three activated finite faults in the dip direction (Figure 5c), we found that the shape of the combined source runup is mainly governed by the interaction between the finite fault showing the largest maximum source runup value (hereafter fault 1) and the other finite faults (hereafter fault 2 and fault 3, respectively). Thus, we modeled the combined source runup ($\bar{S}(x)^j$) by combining the interaction between fault 1 and fault 2 and the interaction between fault 1 and fault 3 and then subtracting the source runup of fault 1 that is considered twice.

$$\bar{S}(x)^j = \sum_{i=2}^{3} \bar{S}(x)^j_{1,i} - S(x)^j_1 \tag{9}$$

where $\bar{S}(x)^j_{1,i}$ is the combined source runup considering the interaction of tsunami waves caused by fault 1 and other finite faults (that can be estimated by Eq. (7)), and $S(x)^j_1$ is the source runup of the fault 1 (that is estimated in the first step).

2.2.3 Step 3

The third step is to estimate the total source runup $S^T(x)$ based on the combined source runups estimated in step 2. This step is divided into two scenarios depending on the distance (D) between the maximum value locations in x direction of the combined source runups.

First, if the distance D is longer than the finite fault length LEN ($D > LEN$, see Figure 6a), the total source runup $S^T(x)$ is the maximum envelope between two combined source runups.

Second, if the distance D is equal to the finite fault length LEN ($D = LEN$, see Figure 6b), the total source runup $S^T(x)$ is not equal to the maximum of two combined source runups due to the interaction of tsunami waves. We characterized the total source runup considering the interaction of tsunami waves by introducing an interaction term $I(x)^{STR}$.

$$S^T(x) = \bar{S}(x)_{max} + I(x)^{STR} \cdot \bar{S}(x)_{min} \tag{10}$$

where $\bar{S}(x)_{max}$ and $\bar{S}(x)_{min}$ are the maximum and minimum envelopes between two combined source runups, respectively. The $I(x)^{STR}$ is the interaction term that determines the ratio of adding total source runup in the overlapping part between two combined source runups.

$$I(x)^{STR} = \gamma \tag{11}$$

where γ is a site-specific coefficient that needs to be calibrated in advance using additional physics-based simulations (see Section 2.3). Note that two activated finite faults do not necessarily need to be adjacent to each other to apply Eqs. (10) and (11), such as the case where 24b and 25z (see Figure 2) are activated.

If there are more than two combined source runups where the distance D is equal to the finite fault length LEN (Figure 6c), the total source runup $S^T(x)$ can be estimated.

$$S^T(x) = \sum_{i=1}^{N-1} S^T(x)^{i,i+1} - \sum_{i=2}^{N-1} \bar{S}(x)^i \tag{12}$$

where $S^T(x)^{i,i+1}$ is the total source runup when considering only two combined source runups. $\bar{S}(x)^i$ is the combined source runup. N is the total number of the combined source runups where the distance D is equal to the finite fault length LEN.

If two scenarios ($D > LEN$ and $D = LEN$) are mixed, the combined source runups ($D = LEN$) are first considered. For example, if four finite faults (24b, 25a, 26a, and 28b) are activated, the source runup due to three activated finite faults (24b, 25a, 26a)

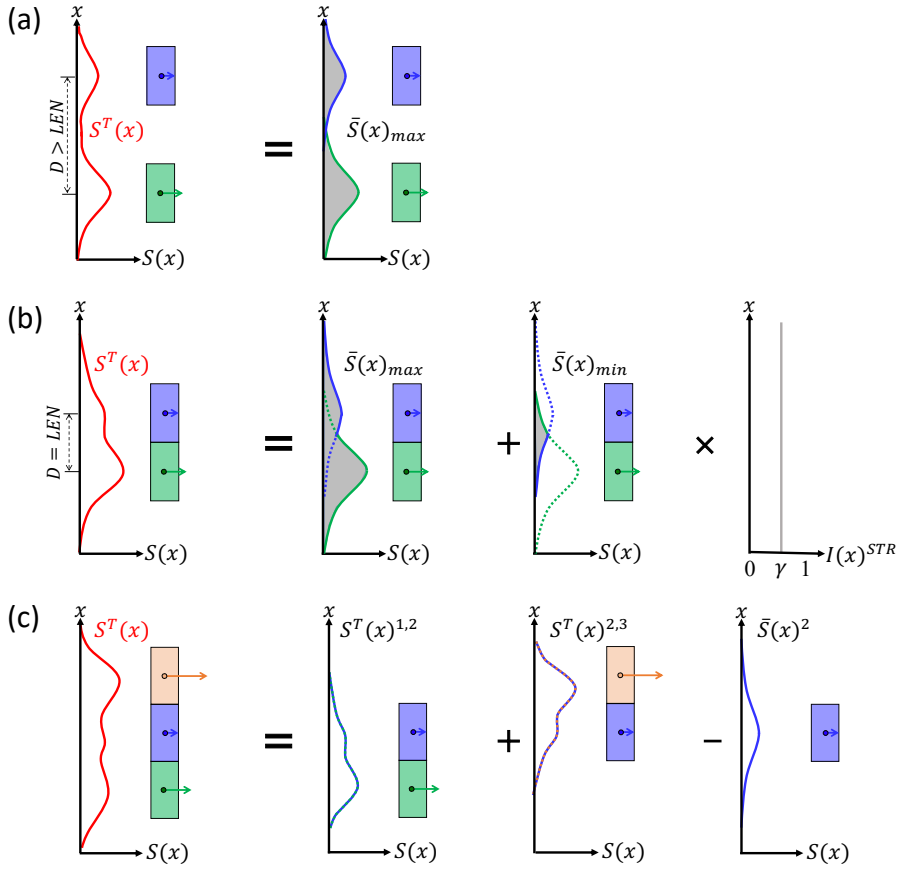

Figure 6. Schematic sketch of step 3 of the prediction process (a) when the distance between the maximum values of the combined source runups is longer than the finite fault length ($D > LEN$), (b) when $D = LEN$, and (c) when there are more than two combined source runups. The red line is the total source runup $S^T(x)$. The rectangles represent the activated finite faults. The gray line represents the interaction term $I(x)^{STR}$.

where $D = LEN$ is first calculated using Eq. (12). Then, the total source runup is defined as the maximum envelope between the source runup of 28b and the estimated source runup due to three activated finite faults (24b, 25a, 26a).

Once the total source runup $S^T(x)$ is estimated, the alongshore tsunami runup distribution $R^p(x)$ –the output of the TRRF-FF model– can be estimated by inputting the total source runup $S^T(x)$ and the normalized topographic runup $NT^p(x)$ to Eq. (6).

2.3 Calibration

As mentioned in Section 2.2, to run the TRRF-FF model, the site-specific coefficients (α, β, and γ) in Eqs. (8, 11) should be determined based on additional physics-based simulations (see Figure 1).

2.3.1 Step 1: α and β

First, to calibrate the α and β in Eq. (8) using the physics-based model Basilisk, we simulated 45 tsunamigenic-earthquake scenarios where two activated finite faults that have the same unit source ID number as in Figure 5b. For each unit source ID (see Fig-

ure 2), there are three combinations to compose two finite faults that have the same unit source ID number (e.g., 24b and 24a, 24a and 24z, 24b and 24z). For each combination, we generated three scenarios by randomly choosing the dip angle, slip, and depth values within the range in Table 2. Note that the samples were drawn from a uniform probability distribution. To make a realistic earthquake scenario that can occur in a subduction zone setting, we constrained the fault closer to Japan to have a larger dip angle than that of the fault farther away from Japan. The depth of the fault closer to Japan was calculated based on the depth and dip angle of the fault farther away from Japan. For each scenario, we predicted the alongshore tsunami runup distribution using the TRRF-FF model as α changes from 0.1 to 3.0, with 0.1 intervals, and as β changes from -0.5 to 1.5, with 0.1 intervals. Then, the Normalized Root Mean Square Error ($NRMSE$), defined as the $RMSE$ normalized by the maximum runup, was calculated (Eq. 13).

$$NRMSE = \frac{\sqrt{\frac{1}{N_p}\sum_{x=1}^{N_p}\left[R^p(x) - R^T(x)\right]^2}}{max\left[R^T(x)\right]} \times 100\,(\%) \tag{13}$$

where $R^p(x)$ is the alongshore tsunami runup distribution predicted by the TRRF-FF model, $R^T(x)$ is the alongshore tsunami runup distribution predicted by Basilisk, and N_p is the number of alongshore locations considered. Figure 7a shows how the mean $NRMSE$, over the 45 scenarios, varies based on α and β. Based on this result, we set the α and β to 1.2 and 0.3, respectively, which combination shows the minimum mean $NRMSE$ (mean $NRMSE$=7.72%, 95% confidence interval: 7.19%, 8.25%). The α (= 1.2) indicates that the combined source runup is smaller than the sum of each source runup for a range 20% wider than the width (a_2) of the $S(x)_2^j$ (see Figure 5b). The β (= 0.3) indicates that the combined source runup is smaller than the $S(x)_1^j$ up to 30% of the $S(x)_2^j$ near the center position of the finite fault (see Figure 5b).

2.3.2 Step 2: γ

Secondly, to calibrate the γ of Eq. (11) using Basilisk, we simulated 108 tsunamigenic-earthquake scenarios where two activated finite faults with the unit source ID number different by one as in Figure 6b. Since we considered five unit source numbers (see Figure 2), there are four combinations to compose two finite faults with the unit source ID number different by one (e.g., 24 and 25, 25 and 26, 26 and 27, 27 and 28). For each combination, there are nine possible scenarios (e.g., aa, ab, az, ba, bb, bz, za, zb, zz). For each scenario, we generated three scenarios by randomly choosing the dip angle, slip, and depth values within the range in Table 2. We predicted the alongshore tsunami runup distribution using the TRRF-FF model as γ changes from 0.0 to 1.4, with 0.1 intervals. Then, the $NRMSE$ between the TRRF-FF model prediction and the Basilisk model prediction was calculated (Figure 7b). Based on this result, we set γ to 0.2, corresponding to the minimum mean $NRMSE$ (mean $NRMSE$=7.82%, 95% confidence interval: 7.55%, 8.11%).

3 Performance on synthetic tsunami scenarios

We systemically designed five tests to evaluate the performance of each step of the TRRF-FF model prediction process. Note that the synthetic tsunami scenarios used in each test were never used for TRRF-FF training and calibration. The overall error of the TRRF-FF model in each corresponding test and the example results of each test can be found in Figure 8 and Figure 9, respectively. In the following, we discuss how we designed each test and discuss the performance of the TRRF-FF model.

First, in order to evaluate the performance of step 1 of the TRRF-FF model prediction process, we tested the cases where there is one activated finite fault (Test 1). We generated 45 tsunamigenic-earthquake scenarios (three random scenarios for each finite

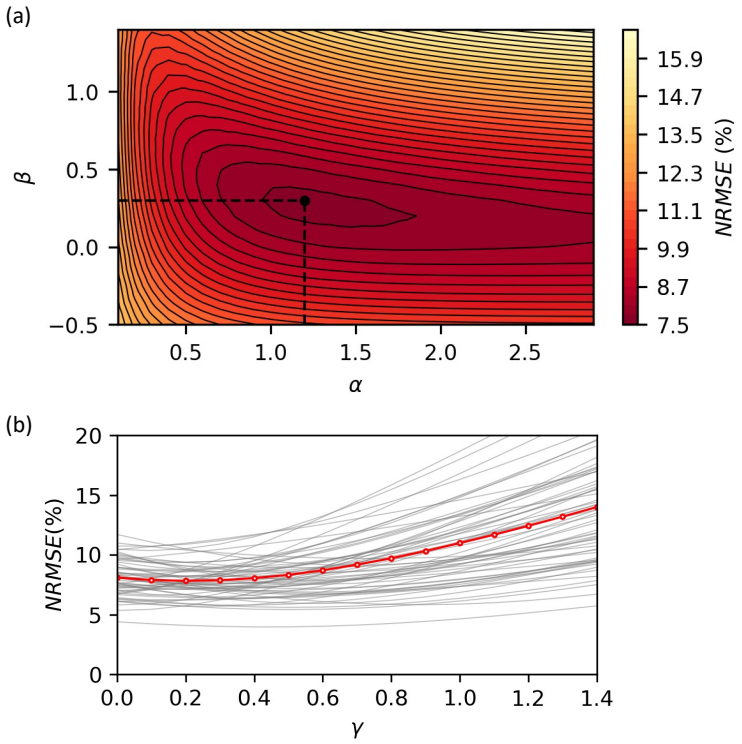

Figure 7. TRRF-FF model calibration results. (a) Mean $NRMSE$ depending on α and β of Eq. (8). The black circle is the location where the $NRMSE$ shows the minimum value. (b) $NRMSE$ depending on γ of Eq. (11). The gray lines represent each tsunamigenic-earthquake scenario result, and the red line with circles represents the mean $NRMSE$.

fault) where the finite fault parameter (dip angle, slip, depth) values were chosen within the range in Table 2.

Second, in order to evaluate the performance of Eq. (7) in step 2 of the TRRF-FF model prediction process, we tested the cases where there are two activated finite faults that have the same unit source ID number (Test 2). We generated 30 tsunamigenic-earthquake scenarios by following the same procedure to calibrate the site-specific coefficients α and β in Section 2.3, but using two random scenarios.

Third, in order to evaluate the performance of Eq. (9) in step 2 of the TRRF-FF model prediction process, we tested 25 tsunamigenic-earthquake scenarios where there are three activated finite faults that have the same unit source ID number (Test 3). There are five cases where three activated finite faults have the same unit source ID number (e.g., 24a, 24b, 24z in Figure 2). For each case, five scenarios were considered by randomly choosing the finite fault parameter (dip angle, slip, depth) values within the range in Table 2. In the same way that the scenarios were generated for calibration, we constrained the fault closer to Japan to have a larger dip angle than that of the fault farther away from Japan.

Fourth, in order to evaluate the performance of Eq. (10) in step 3 of the TRRF-FF model prediction process, we tested the cases where there are two activated finite faults with the unit source ID number different by one (Test 4). We generated 72 tsunamigenic-earthquake scenarios by following the same procedure to calibrate the site-specific coefficient γ in Section 2.3, but using two random scenarios.

Fifth, in order to evaluate the overall performance of the TRRF-FF model prediction process, we tested 50 random tsunamigenic-earthquake scenarios with characteristics similar to the 2011 Tohoku tsunami (Test 5). To generate scenarios similar to the 2011 Tohoku tsunami source of Tang et al. (2012), we randomly chose six finite faults, fixed the moment magnitude (M_W) to 8.81, and constrained the fault closer to Japan to have a larger dip angle than that of the fault farther away from Japan. Note that the moment magnitude (M_W) was calculated assuming that the rigidity modulus is $4{\times}10^{10}\ Nm^{-2}$ in East Japan, following Gica (2008).

Figure 8 shows the $NRMSE$ distribution of each test in a box plot. The Test 1 results (mean $NRMSE = 7.11\%$) confirmed that the performance of the TRRF-FF model based on uniform slip condition in East Japan is similar to the performance of the TRRF model in northern Puerto Rico (J.-W. Lee et al., 2020) and that in northern Chile (J.-W. Lee et al., 2021). The error increases by about 14 percentage points of mean $NRMSE$ if there are more than two activated finite faults (Test 2, Test 3, Test 4, Test 5). Similar errors between Test 2 (mean $NRMSE = 20.90\%$) and Test 3 (mean $NRMSE = 19.18\%$) confirm that Eq. (9) is valid. Also, similar errors between Test 4 (mean $NRMSE = 21.31\%$) and Test 5 (mean $NRMSE = 20.19\%$) confirm the validity of Eq. (12). The similar errors between Test 2 and Test 4 indicate that Eq. (7) and Eq. (10) contribute to similar-magnitude errors.

Figure 9 shows example results of each test that exhibit $NRMSE$ similar to the median $NRMSE$, as depicted in Figure 8. The source runup of Figure 9a shows the shape of the empirical formula in Okal and Synolakis (2004) (see Eq. (2)). As shown in Figure 9b and c, when the activated finite faults have the same unit source ID number, the maximum value of total source runup $S^T(x)$ (red line) is smaller than the maximum of individual source runups $S(x)$ (gray lines) because of the interaction among the finite faults modeled in Eq. (8). On the other hand, when the unit source ID numbers of the activated finite faults are different by one (Figure 9d), the total source runup $S^T(x)$ (red line) is slightly larger than the maximum of the combined source runups $\bar{S}(x)$ because of the interaction between finite faults modeled in Eq. (11). The comparison of alongshore tsunami runup distribution (bottom panels in Figure 9) shows that overall, the TRRF-

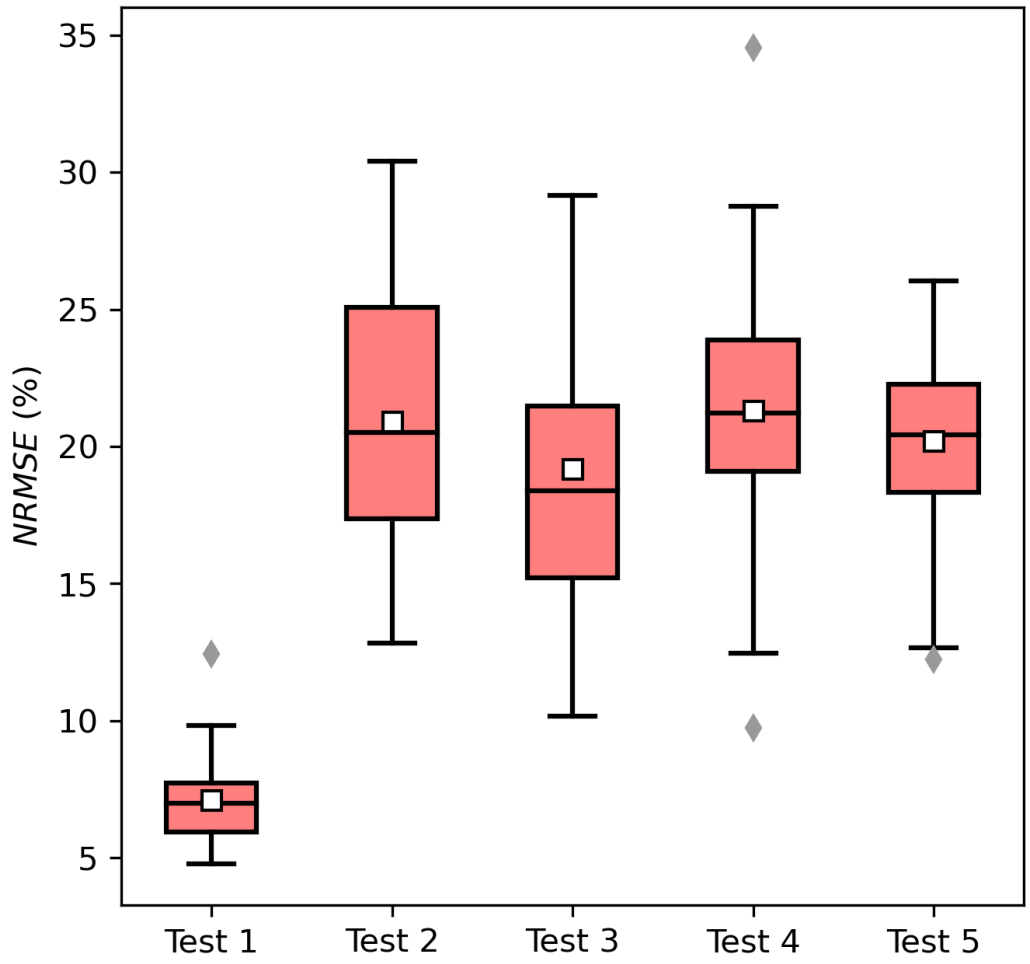

Figure 8. Performance of the TRRF-FF model based on synthetic tsunami scenarios. The box represents the interquartile range, the black lines stretched from the box represent the range of 1.5 times of the interquartile range, and the black line inside the box represents the median. The white rectangle represents the mean. The outlier is represented in a gray diamond.

FF model agrees well in that it captures the shape and magnitude of the alongshore runup distribution. However, there are a few areas where the difference in the runup is more than two-fold (e.g., the area between $36.5°N$ and $38.0°N$ in Figure 9e). These errors may be attributed to the nonlinear behavior of the tsunami wave in complex topography (J.-W. Lee et al., 2020), which is neglected in the TRRF-FF modeling approach.

4 2011 Tohoku Tsunami Event

To evaluate the performance of the TRRF-FF model based on a real tsunami event, we applied the TRRF-FF model to the 2011 Tohoku tsunami event. The M_w 9.0 2011 Tohoku earthquake occurred on March 11, 2011, at 05:46:24 UTC, off the Pacific coast of northeastern Honshu, Japan (see yellow star in Figure 2). The massive tsunamis that inundated several hundred kilometers of northeast Honshu coastlines caused an estimated $300 billion in damage (Tajima et al., 2013). Considering the large rupture area and com-

ID	DIP (°)	DEP (km)	SLP (m)
24b	19	5.0	4.66
25b	19	5.0	12.23
26b	19	5.0	21.27
26a	21	21.3	26.31
27b	19	5.0	2.98
27a	21	21.3	22.75

Table 3. Tang et al. (2012)'s 2011 Tohoku tsunami source. The ID of the unit sources corresponds to Figure 2. DIP is dip angle, DEP is depth, and SLP is slip.

plex earthquake slip distribution, the 2011 Tohoku tsunami event is an appropriate case study to evaluate the forecasting capability of the TRRF-FF model.

We chose the Tang et al. (2012)'s tsunami source that is based on the same unit source geometry used in this study (Figure 10a). The tsunami source is estimated based on two DART measurements within 1.5 hours of the earthquake (Wei et al., 2013) and consists of six activated finite faults with slips of up to 26.31 m (Table 3). Note that this tsunami source was not used for training and calibration. Figure 10b shows the combined source runups $\bar{S}(x)$ (blue lines) and the total source runup $S^T(x)$ (red line). The maximum total source runup $S^T(x)$ was shown near the epicenter latitude. Figure 10c shows a comparison of alongshore tsunami runup distribution between the TRRF-FF model and the physics-based model. The performance of the TRRF-FF model for the 2011 Tohoku tsunami event ($NRMSE = 23.27\%$) was similar to the performance based on the synthetic tsunami scenarios (Figure 8). The results show that the TRRF-FF model slightly overestimates the runups between $37°N$ and $37.5°N$, and underestimates the high runup zone between $38.2°N$ and $39°N$. But overall, the leading order of the TRRF-FF model prediction agrees well with that of the physics-based model prediction. We also compared the TRRF-FF model prediction with the tsunami survey observations of Mori et al. (2011) (Figure 10d). The comparison with these tsunami runup observations shows a tendency of both the TRRF-FF model and the physics-based model to underestimate the runup, especially in the northern area ($> 39°N$). As noted by MacInnes et al. (2013), the underestimation may be attributed to Tang et al. (2012)'s tsunami source, not the TRRF-FF modeling approach, given the results of the physics-based model similarly underestimated the runup. High-resolution bathymetry data (< 50 m) (Shimozono et al., 2012, 2014), Manning's roughness based on the land cover (MacInnes et al., 2013), and three-dimensional tsunami simulation (Kim et al., 2013) may help to reproduce the high observed runups that usually occur at the heads of V-shaped bays, apexes of peninsulas, or narrow inlets.

Several tsunami forecast systems issue warnings, typically classifying the warning as one of only a few levels, such as major tsunami warning, tsunami warning, and tsunami advisory (e.g., Catalan et al., 2020; Hoshiba & Ozaki, 2014). This coarse granularity is necessary because the tsunami runup or amplitude information is too complex to be used directly in communicating tsunami warning (Melgar et al., 2016). Therefore, one of the ways to quantify forecasting performance is to calculate the percentage of tsunami runup correctly predicted within a warning level range. With this viewpoint, we investigated the tsunami forecasting performance of the TRRF-FF model based on the five-level criteria of the Japan Meteorological Agency (JMA) ($0.2 - 1.0m$, $1.0 - 3.0m$, $3.0 - 5.0m$, $5.0 - 10.0m$, $>10.0m$, Kamigaichi, 2022) as an example (Figures 11a and b). We applied runup values to the five-level criteria, which is different from JMA's tsunami warning system that uses maximum tsunami amplitude along the coast. Note that JMA employs the maximum tsunami amplitude information as a tsunami prediction criterion be-

cause Japan has long studied the relationship between tsunami damage and tsunami amplitude along its coast (Kamigaichi, 2022). To quantify the classification accuracy, we plotted the confusion matrix, also called an error matrix or possibility table (Figure 11c). The results show that the predicted warning levels based on the TRRF-FF model agree well with the warning levels based on the physics-based model, although the TRRF-FF model slightly underestimates the warning level in the southern area. The predicted warning levels of the two models were the same at about 68.9% locations, and a one warning level difference was seen at 29.3% locations.

The computational time of the TRRF-FF model was less than a second when a single-core processor was used, while that of the physics-based model was about one hour when a 24-core processor was used. This speed of computing the TRRF-FF model may be similar or shorter than that of the JMA's tsunami warning system that searches the similar earthquake scenarios among about 64,000 scenarios. When the 2011 Tohoku earthquake occurred, JMA issued the initial warnings within three minutes, including tsunami source inversion and tsunami forecasting (Hoshiba & Ozaki, 2014).

5 Discussion

5.1 Flexibility and storage space

One of the advantages of the TRRF-FF model is that the TRRF-FF model can be applied to any combination of finite faults with different fault parameter values (dip angle, depth, and slip), not just the fault parameter values used for training. For this reason, we were able to investigate the performance of the TRRF-FF model based on more than 200 synthetic tsunami scenarios by randomly choosing dip angle, depth, and slip within the range used in training (Section 3). It should be noted that the TRRF-FF model can be applied to the heterogeneous earthquake slip distribution (Test 2 to Test 5 in Figure 8) as well as the uniform earthquake slip distribution (Test 1 in Figure 8). Given that the quality of tsunami predictions can be affected by incorrect assumptions about fault geometry (Tsushima et al., 2014), this flexibility is a significant advantage, allowing the TRRF-FF model to respond to a broader range of tsunami scenarios than approaches that fix the fault geometry. For example, the pre-computed tsunami simulation database of JMA's tsunami warning system only considers different hypocenter locations, focal depth, and magnitude (Hoshiba & Ozaki, 2014). The Near-field Tsunami Inundation Forecasting (NearTIF) method (Gusman et al., 2014) only takes the tsunami scenario into account for which the dip angle and depth values are fixed to the SLAB model (Hayes et al., 2012).

Moreover, the TRRF-FF model can be applied to any other finite fault position. If the finite fault position that is different from the finite fault location used for training is used, the TRRF-FF model finds the nearest finite fault location used for training from the activated finite fault. The TRRF-FF model adjusts the X value in Eq. (2) by the distance between the activated finite fault location and the nearest finite fault location, in the direction parallel to the coastline. Also, the TRRF-FF model adjusts the Y values in Eq. (3) and Eq. (4) by the distance between the activated finite fault location and the nearest finite fault location, in the direction perpendicular to the coastline. In Section 3, we only tested the performance of the TRRF-FF model based on those synthetic scenarios where all positions of the activated finite faults were fixed to the finite fault locations used for training (Figure 2), given that the finite fault locations are usually fixed in tsunami forecasting in order to infer a tsunami source from recorded waveforms as rapidly as possible. However, if the tsunami warning needs to be updated based on a slip distribution that is inferred from different finite fault locations, the ability to apply the TRRF-FF model to other finite fault locations is necessary. To investigate the performance of the TRRF-FF model for any finite fault location, we simulated two scenarios where the Tang et al. (2012)'s slip distribution is shifted by 0.5° to the west and

to the south, respectively (Figure 12). Although the runup between $37°N$ and $38°N$ did not match well in these cases, the results showed similar or even better performance than the 2011 Tohoku tsunami case (Figure 10c), confirming the ability of the TRRF-FF model to handle other finite fault locations not used for training.

Another advantage of the TRRF-FF model is that the trained TRRF-FF model takes up less than one megabyte of storage space. If the algorithm is optimized and visualization is not required, the TRRF-FF model will take up much less storage space than one megabyte. This lightweight model size is a significant advantage that makes the TRRF-FF model easy to implement and manage on affordable computers. On the other hand, for example, the tsunami forecasting system based on a pre-computed tsunami simulation database in the North-eastern Atlantic, the Mediterranean, and connected seas requires about 30 terabytes of storage space (Selva et al., 2021). This large storage space could be a critical factor when building a tsunami forecasting system in a country that cannot afford large-capacity storage.

5.2 Computational speed and reliability

Along with the flexibility and the storage space of the TRRF-FF model, we emphasize the computational speed and reliability of the TRRF-FF model. The computational time needed for the TRRF-FF model to predict runup for one scenario was less than a second (on a single-core processor), while that of the physics-based model was about 1 hour (on average on a 24-core processor). Thanks to its rapid computational speed, we believe that the TRRF-FF model has the potential to be applied within a probabilistic tsunami forecasting framework (Selva et al., 2021) and a probabilistic tsunami hazard assessment framework (Grezio et al., 2017), taking into account uncertainty caused by unknown details of the tsunami source. This is a big advantage of the TRRF-FF model, given that the rupture extent is unknown prior to rupture and the finite fault models have significant epistemic uncertainty (Cienfuegos et al., 2018). Figure 13 shows examples of the probabilistic distribution of alongshore tsunami runup using the TRRF-FF model. We tested how the alongshore tsunami runup distribution changes when the slip uncertainty of the tsunami source of Tang et al. (2012) is 2 m, 4 m, and 6 m, respectively. We generated 1000 scenarios by adding the tsunami source of Tang et al. (2012) and uncertainties sampled from a uniform distribution for each activated finite fault and constrained the slip to a positive value to avoid unrealistic scenarios.

Moreover, the TRRF-FF model prediction process was always stable, since the model solves only well-behaved, simple algebraic equations. On the other hand, a few physics-based model simulations executed to complete this study had some numerical stability issues. The possibility of encountering such instability issues in real-time is a critical concern in tsunami forecasting, as mentioned in Section 1.

5.3 Normalized topographic runup

The TRRF-FF modeling approach assumed that the alongshore tsunami runup distribution could be expressed as a function of the source runup and normalized topographic runup (Eq. (6)). In this form, the normalized topographic runup $NT^p(x)$ is independent of the tsunami source and only related to local topography (Figure 4). A location with a $NT^p(x)$ value greater than zero can be interpreted as an area where a higher runup occurs, compared to a location with a value of zero or less than zero, regardless of the earthquake's characteristics. To elucidate the underlying relationship between the normalized topographic runup $NT^p(x)$ and local topographic features, we compared the normalized topographic runup $NT^p(x)$ with the region's coastline and nearshore slope and found the following two characteristics (Figure 14).

First, the leading-order trend of $NT^p(x)$ (thick black line in Figure 14b) is correlated with the coastline curvature (Figure 14a). We defined the leading-order trend of $NT^p(x)$ as a moving average of $NT^p(x)$. At large spatial scales, the concave-seaward region (e.g., large bay) shows a relatively smaller $NT^p(x)$ value compared to the convex-seaward region (e.g., headland), reflecting the divergence of tsunami waves by refraction. Moreover, relatively large $NT^p(x)$ values are shown in the apexes of peninsulas (red lines in Figure 14b). For example, the $NT^p(x)$ of the concave and low-lying bight along the Sendai plain (the region around $38.0°N$ and $38.3°N$) is about zero, while the $NT^p(x)$ in Minami-Soma (near $37.6°N$) is larger than zero due to the convex shape of the coastline. Published results (e.g., Sato et al., 2014) tell a consistent interpretation based on the tsunami height records in Minami-Soma for the 2011 Tohoku tsunami. However, there is one region where this characteristic does not fit. The $NT^p(x)$ near the Sanriku Coast (the region between $39.0°N$ and $40.5°N$) was smaller than that of the nearby region despite the shape of the convex coastline. We believe this is due to the complex topography near the Sanriku coast combined with the narrow shelf offshore (see Figure 14a).

Second, the extent of local change of $NT^p(x)$ (Figure 14c) is correlated with that of the nearshore slope (Figure 14d). We extracted the extent of local change of $NT^p(x)$ by subtracting the moving averaged normalized topographic runup from the normalized topographic runup (filtered $NT(x)$). We used the nearshore slope information of Athanasiou et al. (2019), which was calculated as the ratio between the cross-shore location of the depth of closure and the cross-shore location of the shoreline. Athanasiou et al. (2019) calculated the depth of closure using the formulation of Nicholls et al. (1998). As shown in the yellow areas in Figure 14c and d, both the extent of local change of $NT^p(x)$ and the variation of the nearshore slope were significant along the Sanriku Coast (the region between $38.2°N$ and $40.5°N$), reflecting a complex tsunami runup process in response to the complex topography.

The pattern of the normalized topographic runup may be related to other topographic features, such as the small islands in the vicinity of the mainland, which can act as a focusing lens of wave energy and amplify runup along the mainland adjacent to the islands (Hill et al., 2012; Stefanakis et al., 2014). Moreover, the pattern of the normalized topographic runup may be related to the tsunami resonance (Abe, 2005; Shimozono et al., 2014; Y. Wang, Zamora, et al., 2021) and the large-scale edge waves trapped by the continental shelf (Watanabe et al., 2012; Yamazaki et al., 2013), which can amplify tsunami waves at the local level.

5.4 Future work

To improve the accuracy and the applicability of the TRRF-FF model, future research should focus on the following limitations.

First, the TRRF-FF model is only applicable to reverse faulting events in the subduction zone. Although seismic slip on offshore megathrusts causes most of the devastating tsunamis (Lindsey et al., 2021), outer rise normal faulting events (e.g., Lay et al., 2011; Okal et al., 2010) and strike-slip events (e.g., Ishii et al., 2013; D. Wang et al., 2012), even without coseismic underwater landslides (Elbanna et al., 2021), can also induce tsunamis, as described in Melgar et al. (2016). Moreover, according to the global historical tsunami database at the National Geophysical Data Center, aside from earthquakes, tsunamis have been generated by landslides, volcanic eruptions, meteorological causes, or a combination of several tsunami sources (Levin et al., 2009). The 2018 Anak Krakatoa (Indonesia) volcanic tsunami (Heidarzadeh et al., 2020; Muhari et al., 2019) and the recent eruption of the Hunga Tonga-Hunga Ha'apai underwater volcano in 2022 (Carvajal et al., 2022) have shown how volcanic activity can also cause devastating tsunamis. Thus, future studies should improve the TRRF-FF model to consider a range of types of tsunami sources.

Second, several other components need to be considered in future studies. For example, the TRRF-FF model can only provide alongshore tsunami runup distribution. However, along with the tsunami runup information, arrival time and inundation distance are critical pieces of information in tsunami forecasting (V. V. Titov et al., 2005). Thus, the TRRF-FF model should be improved to consider this tsunami information in a future study.

Third, although linear superposition of water level from separate tide and tsunami predictions may be valid in permanently submerged areas, for example in tide gauge locations (V. Titov et al., 2016), nonlinear tsunami-tide interactions in the overland tsunami inundation process are highly significant (e.g., H. S. Lee et al., 2015; Zhang et al., 2011); therefore, incorporating the tide component into the TRRF-FF model may be important to consider in future studies.

Fourth, there may be limitations in applying the TRRF-FF model to a large area where the Earth's curvature cannot be ignored because the current TRRF-FF modeling approach was derived based on the Cartesian coordinate system.

Fifth, another limitation of the TRRF-FF modeling approach is the inability to use tsunami sources with a unit source format (finite fault size and rupture geometry), which differs from the unit source format used in the training process. For example, in the case of the 2011 tsunami, even if we receive tsunami source information that better matches the observed values, such as the tsunami source of Yamazaki et al. (2018), the tsunami forecast cannot be updated using the TRRF-FF model because of the different finite fault conditions. In this study, the finite fault size was 100 $km \times 50$ km, and the rake angle was fixed to 90 degrees. On the other hand, the finite fault size of Yamazaki et al. (2018) was 40 $km \times 40$ km, and the rake angle of each finite fault was not fixed to 90 degrees.

And last but not least, we followed the empirical formula proposed by Okal and Synolakis (2004) to characterize the shape of the interaction term (Eq. (8)). Although the validity of adopting Eq. (8) was demonstrated in terms of accuracy in Section 3, there is no physical or statistical basis for adopting Eq. (8). It would be interesting to test various formulas with physical or statistical basis, such as the Gaussian function, to find the optimized formula representing the interaction term.

6 Conclusions

In this study, we presented the TRRF-FF model that can rapidly predict the alongshore tsunami runup distribution from a heterogeneous earthquake slip distribution. The novelty of the proposed method lies in modeling the interaction between finite faults based on a leading-order contribution of the alongshore tsunami runup distribution by extending the TRRF modeling approach of J.-W. Lee et al. (2020). Once the TRRF-FF model is trained and calibrated based on a discrete set of physics-based simulations, the alongshore tsunami runup distribution can be estimated in less than a second for any combination of finite faults with different fault parameter values. We validated the TRRF-FF model based on more than 200 synthetic tsunami events ($M_W \geq 7.9$) in East Japan. Moreover, to demonstrate its forecasting ability, we conducted a retrospective forecast test for the 2011 Tohoku tsunami event using Tang et al. (2012)'s tsunami source and compared the estimated alongshore tsunami runup distribution with the observations (Mori et al., 2011). The results showed that the TRRF-FF model is more flexible and takes up less storage space than the pre-computed tsunami simulation database, as well as being faster and more reliable than the physics-based numerical model. We believe that the TRRF-FF model can support real-time tsunami forecasting by predicting alongshore tsunami runup distribution from a heterogeneous earthquake slip distribution rapidly, accurately, and reliably.

Data availability Statement

The Basilisk model used to simulate tsunamis is available at `http://basilisk.fr/`. The bathymetry data of the General Bathymetric Chart of the Ocean (GEBCO) is available at `https://www.gebco.net/data_and_products/gridded_bathymetry_data/`. The TRRF-FF model used in this paper can be accessed via repository: `https://doi.org/10.17603/ds2-8zjk-t806`.

Acknowledgments

This material is based upon work partially supported by the National Science Foundation under Grant Nos. 1630099 and 1735139. Any opinions, findings, and conclusions or recommendations expressed in this material are those of the authors and do not necessarily reflect the views of the National Science Foundation. The authors acknowledge Advanced Research Computing at Virginia Tech for providing computational resources and technical support that have contributed to the results reported within this paper. URL: https://arc.vt.edu/

References

Abe, K. (2005). Tsunami Resonance Curve from Dominant Periods Observed in Bays of Northeastern Japan. In K. Satake (Ed.), *Tsunamis: Case Studies and Recent Developments* (pp. 97–113). Springer Netherlands. doi: 10.1007/1-4020-3331-1_6

Athanasiou, P., van Dongeren, A., Giardino, A., Vousdoukas, M., Gaytan-Aguilar, S., & Ranasinghe, R. (2019). Global distribution of nearshore slopes with implications for coastal retreat. *Earth System Science Data*, *11*(4), 1515–1529. doi: 10.5194/essd-11-1515-2019

Blewitt, G., Hammond, W., Kreemer, C., Plag, H., Stein, S., & Okal, E. (2009). GPS for real-time earthquake source determination and tsunami warning systems. *Journal of Geodesy*, *83*(3-4), 335–343. doi: 10.1007/s00190-008-0262-5

Blewitt, G., Kreemer, C., Hammond, W. C., Plag, H.-P., Stein, S., & Okal, E. (2006). Rapid determination of earthquake magnitude using GPS for tsunami warning systems. *Geophysical Research Letters*, *33*(11). doi: 10.1029/2006GL026145

Carvajal, M., Sepúlveda, I., Gubler, A., & Garreaud, R. (2022). Worldwide Signature of the 2022 Tonga Volcanic Tsunami. *Geophysical Research Letters*, *49*(6), e2022GL098153. doi: 10.1029/2022GL098153

Catalan, P. A., Gubler, A., Cañas, J., Zuñiga, C., Zelaya, C., Pizarro, L., ... Cienfuegos, R. (2020). Design and operational implementation of the integrated tsunami forecast and warning system in Chile (SIPAT). *Coastal Engineering Journal*, *62*(3), 373-388. doi: 10.1080/21664250.2020.1727402

Cienfuegos, R., Catalán, P. A., Urrutia, A., Benavente, R., Aránguiz, R., & González, G. (2018). What can we do to forecast tsunami hazards in the near field given large epistemic uncertainty in rapid seismic source inversions? *Geophysical Research Letters*, *45*(10), 4944-4955. doi: 10.1029/2018GL076998

Elbanna, A., Abdelmeguid, M., Ma, X., Amlani, F., Bhat, H. S., Synolakis, C., & Rosakis, A. J. (2021). Anatomy of strike-slip fault tsunami genesis. *Proceedings of the National Academy of Sciences*, *118*(19). doi: 10.1073/pnas.2025632118

Fauzi, A., & Mizutani, N. (2020). Machine learning algorithms for real-time tsunami inundation forecasting: A case study in Nankai region. *Pure and Applied Geophysics*, *177*(3), 1437-1450. doi: 10.1007/s00024-019-02364-4

GEBCO Compilation Group. (2019). *Gebco 2019 grid.* doi: 10.5285/836f016a-33be-6ddc-e053-6c86abc0788e

Geist, E. L. (2002). Complex earthquake rupture and local tsunamis. *Journal of Geophysical Research: Solid Earth*, *107*(B5), ESE 2-1-ESE 2-15. doi: 10.1029/

2000JB000139

Gica, E. (2008). *Development of the forecast propagation database for NOAA's short-term inundation forecast for tsunamis (SIFT).* Retrieved from `https://repository.library.noaa.gov/view/noaa/11079` (Technical Memorandum)

Gica, E. (2015). *A tsunami forecast model for Midway Atoll.* Retrieved from `https://repository.library.noaa.gov/view/noaa/11177` (Technical Report) doi: 10.7289/V5RJ4GCP

Greenslade, D. J., Allen, S. C., & Simanjuntak, M. A. (2011). An evaluation of tsunami forecasts from the T2 scenario database. *Pure and Applied Geophysics*, *168*(6), 1137–1151. doi: 10.1007/s00024-010-0229-3

Grezio, A., Babeyko, A., Baptista, M. A., Behrens, J., Costa, A., Davies, G., ... Thio, H. K. (2017). Probabilistic tsunami hazard analysis: Multiple sources and global applications. *Reviews of Geophysics*, *55*(4), 1158-1198. doi: 10.1002/2017RG000579

Gusman, A. R., & Tanioka, Y. (2015). Effectiveness of real-time near-field tsunami inundation forecasts for tsunami evacuation in Kushiro City, Hokkaido, Japan. In V. Santiago-Fandiño, Y. Kontar, & Y. Kaneda (Eds.), *Post-tsunami hazard: Reconstruction and restoration* (pp. 157–177). Cham: Springer International Publishing. doi: 10.1007/978-3-319-10202-3_11

Gusman, A. R., Tanioka, Y., MacInnes, B. T., & Tsushima, H. (2014). A methodology for near-field tsunami inundation forecasting: Application to the 2011 Tohoku tsunami. *Journal of Geophysical Research: Solid Earth*, *119*(11), 8186-8206. doi: 10.1002/2014JB010958

Harig, S., Immerz, A., Weniza, Griffin, J., Weber, B., Babeyko, A., ... Weber, R. (2020). The Tsunami Scenario Database of the Indonesia Tsunami Early Warning System (InaTEWS): Evolution of the Coverage and the Involved Modeling Approaches. *Pure and Applied Geophysics*, *177*(3), 1379–1401. doi: 10.1007/s00024-019-02305-1

Hayes, G. P., Wald, D. J., & Johnson, R. L. (2012). Slab1.0: A three-dimensional model of global subduction zone geometries. *Journal of Geophysical Research: Solid Earth*, *117*(B1). doi: 10.1029/2011JB008524

Heidarzadeh, M., Ishibe, T., Sandanbata, O., Muhari, A., & Wijanarto, A. B. (2020). Numerical modeling of the subaerial landslide source of the 22 December 2018 Anak Krakatoa volcanic tsunami, Indonesia. *Ocean Engineering*, *195*, 106733. doi: 10.1016/j.oceaneng.2019.106733

Hill, E. M., Borrero, J. C., Huang, Z., Qiu, Q., Banerjee, P., Natawidjaja, D. H., ... Sieh, K. (2012). The 2010 Mw 7.8 Mentawai earthquake: Very shallow source of a rare tsunami earthquake determined from tsunami field survey and near-field GPS data. *Journal of Geophysical Research: Solid Earth*, *117*(B6). doi: 10.1029/2012JB009159

Hoshiba, M., & Ozaki, T. (2014). Earthquake early warning and tsunami warning of the Japan Meteorological Agency, and their performance in the 2011 off the Pacific Coast of Tohoku Earthquake (MW9.0). In F. Wenzel & J. Zschau (Eds.), *Early warning for geological disasters: Scientific methods and current practice* (pp. 1–28). Berlin, Heidelberg: Springer Berlin Heidelberg. doi: 10.1007/978-3-642-12233-0_1

Igarashi, Y., Kong, L., Yamamoto, M., & McCreery, C. S. (2011). Anatomy of historical tsunamis: Lessons learned for tsunami warning. *Pure and Applied Geophysics*, *168*(11), 2043-2063. doi: 10.1007/s00024-011-0287-1

Inoue, T., Abe, T., Koshimura, S., Musa, A., Murashima, Y., & Kobayashi, H. (2019). Development and validation of a tsunami numerical model with the polygonally nested grid system and its MPI-parallelization for real-time tsunami inundation forecast on a regional scale. *Journal of Disaster Research*, *14*(3), 416-434. doi: 10.20965/jdr.2019.p0416

Ishii, M., Kiser, E., & Geist, E. L. (2013). Mw 8.6 Sumatran earthquake of 11 April 2012: Rare seaward expression of oblique subduction. *Geology*, *41*(3), 319-322. doi: 10.1130/G33783.1

Kamigaichi, O. (2022). Tsunami forecasting and warning. *Complexity in Tsunamis, Volcanoes, and their Hazards*, 335–371.

Kim, D. C., Kim, K. O., Pelinovsky, E., Didenkulova, I., & Choi, B. H. (2013). Three-dimensional tsunami runup simulation for the port of Koborinai on the Sanriku coast of Japan. *Journal of Coastal Research*(65 (10065)), 266-271. doi: 10.2112/SI65-046.1

Lauterjung, J., Rudloff, A., Münch, U., & Acksel, D. J. (2014). The earthquake and tsunami early warning system for the Indian Ocean (GITEWS). In F. Wenzel & J. Zschau (Eds.), *Early warning for geological disasters: Scientific methods and current practice* (pp. 165–178). Berlin, Heidelberg: Springer Berlin Heidelberg. doi: 10.1007/978-3-642-12233-0_9

Lay, T., Ammon, C. J., Kanamori, H., Kim, M. J., & Xue, L. (2011). Outer trench-slope faulting and the 2011 Mw 9.0 off the Pacific coast of Tohoku Earthquake. *Earth, Planets and Space*, *63*(7), 37. doi: 10.5047/eps.2011.05.006

Lee, H. S., Shimoyama, T., & Popinet, S. (2015). Impacts of tides on tsunami propagation due to potential Nankai Trough earthquakes in the Seto Inland Sea, Japan. *Journal of Geophysical Research: Oceans*, *120*(10), 6865-6883. doi: 10.1002/2015JC010995

Lee, J.-W., Irish, J. L., & Weiss, R. (2020). Rapid prediction of alongshore run-up distribution from near-field tsunamis. *Natural Hazards*, *104*(2), 1157–1180. doi: 10.1007/s11069-020-04209-z

Lee, J.-W., Irish, J. L., & Weiss, R. (2021). Probabilistic near-field tsunami source and tsunami run-up distribution inferred from tsunami run-up records in northern Chile. *Journal of Geophysical Research: Oceans*, *126*(6), e2021JC017289. doi: doi.org/10.1029/2021JC017289

LeVeque, R. J., Waagan, K., González, F. I., Rim, D., & Lin, G. (2016). Generating random earthquake events for probabilistic tsunami hazard assessment. *Pure and Applied Geophysics*, *173*(12), 3671-3692. doi: 10.1007/s00024-016-1357-1

Levin, B. W., Nosov, M., et al. (2009). *Physics of tsunamis* (Vol. 2016). Springer. doi: 10.1007/978-3-319-24037-4

Li, L., Switzer, A. D., Chan, C.-H., Wang, Y., Weiss, R., & Qiu, Q. (2016). How heterogeneous coseismic slip affects regional probabilistic tsunami hazard assessment: A case study in the South China Sea. *Journal of Geophysical Research: Solid Earth*, *121*(8), 6250-6272. doi: 10.1002/2016JB013111

Lindsey, E. O., Mallick, R., Hubbard, J. A., Bradley, K. E., Almeida, R. V., Moore, J. D. P., ... Hill, E. M. (2021). Slip rate deficit and earthquake potential on shallow megathrusts. *Nature Geoscience*, *14*(5), 321-326. doi: 10.1038/s41561-021-00736-x

Løvholt, F., Lorito, S., Macias, J., Volpe, M., Selva, J., & Gibbons, S. (2019). Urgent tsunami computing. In *2019 ieee/acm hpc for urgent decision making (urgenthpc)* (p. 45-50). doi: 10.1109/UrgentHPC49580.2019.00011

MacInnes, B. T., Gusman, A. R., LeVeque, R. J., & Tanioka, Y. (2013). Comparison of earthquake source models for the 2011 Tohoku event using tsunami simulations and near-field observations. *Bulletin of the Seismological Society of America*, *103*(2B), 1256-1274. doi: 10.1785/0120120121

Maeda, T., Obara, K., Shinohara, M., Kanazawa, T., & Uehira, K. (2015). Successive estimation of a tsunami wavefield without earthquake source data: A data assimilation approach toward real-time tsunami forecasting. *Geophysical Research Letters*, *42*(19), 7923-7932. doi: https://doi.org/10.1002/2015GL065588

Melgar, D., Allen, R. M., Riquelme, S., Geng, J., Bravo, F., Baez, J. C., ... Smalley Jr., R. (2016). Local tsunami warnings: Perspectives from re-

cent large events. *Geophysical Research Letters*, *43*(3), 1109-1117. doi: 10.1002/2015GL067100

Melgar, D., & Bock, Y. (2013). Near-field tsunami models with rapid earthquake source inversions from land- and ocean-based observations: The potential for forecast and warning. *Journal of Geophysical Research: Solid Earth*, *118*(11), 5939-5955. doi: https://doi.org/10.1002/2013JB010506

Mori, N., Takahashi, T., Yasuda, T., & Yanagisawa, H. (2011). Survey of 2011 Tohoku earthquake tsunami inundation and run-up. *Geophysical Research Letters*, *38*(7). doi: 10.1029/2011GL049210

Mueller, C., Power, W., Fraser, S., & Wang, X. (2015). Effects of rupture complexity on local tsunami inundation: Implications for probabilistic tsunami hazard assessment by example. *Journal of Geophysical Research: Solid Earth*, *120*(1), 488-502. doi: 10.1002/2014JB011301

Muhari, A., Heidarzadeh, M., Susmoro, H., Nugroho, H. D., Kriswati, E., Supartoyo, ... Arikawa, T. (2019). The December 2018 Anak Krakatau Volcano Tsunami as inferred from post-tsunami field surveys and spectral analysis. *Pure and Applied Geophysics*, *176*(12), 5219-5233. doi: 10.1007/s00024-019-02358-2

Mulia, I. E., Gusman, A. R., & Satake, K. (2018). Alternative to non-linear model for simulating tsunami inundation in real-time. *Geophysical Journal International*, *214*(3), 2002-2013. doi: 10.1093/gji/ggy238

Mulia, I. E., Gusman, A. R., & Satake, K. (2020). Applying a deep learning algorithm to tsunami inundation database of megathrust earthquakes. *Journal of Geophysical Research: Solid Earth*, *125*(9), e2020JB019690. doi: 10.1029/2020JB019690

Mulia, I. E., Ueda, N., Miyoshi, T., Gusman, A. R., & Satake, K. (2022, Sep 19). Machine learning-based tsunami inundation prediction derived from offshore observations. *Nature Communications*, *13*(1), 5489. doi: 10.1038/s41467-022-33253-5

Musa, A., Watanabe, O., Matsuoka, H., Hokari, H., Inoue, T., Murashima, Y., ... Kobayashi, H. (2018). Real-time tsunami inundation forecast system for tsunami disaster prevention and mitigation. *The Journal of Supercomputing*, *74*(7), 3093-3113. doi: 10.1007/s11227-018-2363-0

National Research Council. (2011). *Tsunami warning and preparedness: An assessment of the U.S. tsunami program and the nation's preparedness efforts*. Washington, DC: The National Academies Press. doi: 10.17226/12628

Nicholls, R. J., Birkemeier, W. A., & hong Lee, G. (1998). Evaluation of depth of closure using data from Duck, NC, USA. *Marine Geology*, *148*(3), 179-201. doi: 10.1016/S0025-3227(98)00011-5

Ohta, Y., Kobayashi, T., Tsushima, H., Miura, S., Hino, R., Takasu, T., ... Umino, N. (2012). Quasi real-time fault model estimation for near-field tsunami forecasting based on RTK-GPS analysis: Application to the 2011 Tohoku-Oki earthquake (Mw 9.0). *Journal of Geophysical Research: Solid Earth*, *117*(B2). doi: https://doi.org/10.1029/2011JB008750

Oishi, Y., Imamura, F., & Sugawara, D. (2015). Near-field tsunami inundation forecast using the parallel TUNAMI-N2 model: Application to the 2011 Tohoku-Oki earthquake combined with source inversions. *Geophysical Research Letters*, *42*(4), 1083-1091. doi: doi.org/10.1002/2014GL062577

Okada, Y. (1985). Surface deformation due to shear and tensile faults in a half-space. *Bulletin of the seismological society of America*, *75*(4), 1135–1154.

Okal, E. A., Fritz, H. M., Synolakis, C. E., Borrero, J. C., Weiss, R., Lynett, P. J., ... Chan, I.-c. (2010). Field Survey of the Samoa Tsunami of 29 September 2009. *Seismological Research Letters*, *81*(4), 577-591. doi: 10.1785/gssrl.81.4.577

Okal, E. A., & Synolakis, C. E. (2004). Source discriminants for near-field tsunamis. *Geophysical Journal International*, *158*(3), 899–912. doi: 10.1111/j.1365-246X

.2004.02347.x

Popinet, S. (2015). A quadtree-adaptive multigrid solver for the Serre–Green–Naghdi equations. *Journal of Computational Physics*, *302*, 336–358. doi: 10.1016/j.jcp.2015.09.009

Saito, T., Satake, K., & Furumura, T. (2010). Tsunami waveform inversion including dispersive waves: the 2004 earthquake off Kii Peninsula, Japan. *Journal of Geophysical Research: Solid Earth*, *115*(B6). doi: 10.1029/2009JB006884

Sato, S., Okayasu, A., Yeh, H., Fritz, H. M., Tajima, Y., & Shimozono, T. (2014). Delayed survey of the 2011 Tohoku Tsunami in the former exclusion zone in Minami-Soma, Fukushima Prefecture. *Pure and Applied Geophysics*, *171*(12), 3229-3240. doi: 10.1007/s00024-014-0809-8

Selva, J., Lorito, S., Volpe, M., Romano, F., Tonini, R., Perfetti, P., ... Amato, A. (2021). Probabilistic tsunami forecasting for early warning. *Nature Communications*, *12*(1), 5677. doi: 10.1038/s41467-021-25815-w

Setiyono, U., Gusman, A. R., Satake, K., & Fujii, Y. (2017). Pre-computed tsunami inundation database and forecast simulation in Pelabuhan Ratu, Indonesia. *Pure and Applied Geophysics*, *174*(8), 3219-3235. doi: 10.1007/s00024-017-1633-8

Shimozono, T., Cui, H., Pietrzak, J. D., Fritz, H. M., Okayasu, A., & Hooper, A. J. (2014). Short wave amplification and extreme runup by the 2011 Tohoku Tsunami. *Pure and Applied Geophysics*, *171*(12), 3217-3228. doi: 10.1007/s00024-014-0803-1

Shimozono, T., Sato, S., Okayasu, A., Tajima, Y., Fritz, H. M., Liu, H., & Takagawa, T. (2012). Propagation and inundation characteristics of the 2011 Tohoku Tsunami on the Central Sanriku Coast. *Coastal Engineering Journal*, *54*(1), 1250004-1-1250004-17. doi: 10.1142/S0578563412500040

Stefanakis, T. S., Contal, E., Vayatis, N., Dias, F., & Synolakis, C. (2014). Can small islands protect nearby coasts from tsunamis? An active experimental design approach. *Proceedings of the Royal Society A: Mathematical, Physical and Engineering Sciences*, *470*(2172), 20140575. doi: 10.1098/rspa.2014.0575

Tajima, F., Mori, J., & Kennett, B. L. (2013). A review of the 2011 Tohoku-Oki earthquake (Mw 9.0): Large-scale rupture across heterogeneous plate coupling. *Tectonophysics*, *586*, 15-34. (Recent Megathrust Earthquakes and Tsunamis: Observations and Processes) doi: doi.org/10.1016/j.tecto.2012.09.014

Tang, L., Titov, V. V., Bernard, E. N., Wei, Y., Chamberlin, C. D., Newman, J. C., ... Gica, E. (2012). Direct energy estimation of the 2011 Japan tsunami using deep-ocean pressure measurements. *Journal of Geophysical Research: Oceans*, *117*(C8). doi: 10.1029/2011JC007635

Tanioka, Y., Grillo, U. G., & Arguello, G. J. (2020). Near-real time tsunami inundation forecast for Central America : case study of the 1992 Nicaragua tsunami earthquake. *Coastal Engineering Journal*, *62*(3), 350-361. doi: 10.1080/21664250.2019.1708536

Tanioka, Y., Gusman, A. R., Ioki, K., & Nakamura, Y. (2014). Real-time tsunami inundation forecast for a recurrence of 17th century great Hokkaido earthquake in Japan. *Journal of Disaster Research*, *9*(3), 358-364. doi: 10.20965/jdr.2014.p0358

Thingbaijam, K. K. S., Martin Mai, P., & Goda, K. (2017). New empirical earthquake source-scaling laws. *Bulletin of the Seismological Society of America*, *107*(5), 2225-2246. doi: 10.1785/0120170017

Titov, V., Kânoğlu, U., & Synolakis, C. (2016). Development of MOST for Real-Time Tsunami Forecasting. *Journal of Waterway, Port, Coastal, and Ocean Engineering*, *142*(6), 03116004. doi: 10.1061/(ASCE)WW.1943-5460.0000357

Titov, V. V., Gonzalez, F. I., Bernard, E., Eble, M. C., Mofjeld, H. O., Newman, J. C., & Venturato, A. J. (2005). Real-time tsunami forecasting: Challenges and solutions. *Natural Hazards*, *35*(1), 35–41.

Tsushima, H., Hino, R., Fujimoto, H., Tanioka, Y., & Imamura, F. (2009). Near-field tsunami forecasting from cabled ocean bottom pressure data. *Journal of Geophysical Research: Solid Earth*, *114*(B6). doi: 10.1029/2008JB005988

Tsushima, H., Hino, R., Ohta, Y., Iinuma, T., & Miura, S. (2014). tFISH/RAPiD: Rapid improvement of near-field tsunami forecasting based on offshore tsunami data by incorporating onshore GNSS data. *Geophysical Research Letters*, *41*(10), 3390-3397. doi: 10.1002/2014GL059863

Tsushima, H., Hino, R., Tanioka, Y., Imamura, F., & Fujimoto, H. (2012). Tsunami waveform inversion incorporating permanent seafloor deformation and its application to tsunami forecasting. *Journal of Geophysical Research: Solid Earth*, *117*(B3). doi: 10.1029/2011JB008877

Tsushima, H., Hirata, K., Hayashi, Y., Tanioka, Y., Kimura, K., Sakai, S., ... Maeda, K. (2011). Near-field tsunami forecasting using offshore tsunami data from the 2011 off the Pacific coast of Tohoku Earthquake. *Earth, Planets and Space*, *63*(7), 56. doi: 10.5047/eps.2011.06.052

Tsushima, H., & Ohta, Y. (2014). Review on near-field tsunami forecasting from offshore tsunami data and onshore GNSS data for tsunami early warning. *Journal of Disaster Research*, *9*(3), 339-357. doi: 10.20965/jdr.2014.p0339

Ulutas, E. (2013). Comparison of the seafloor displacement from uniform and non-uniform slip models on tsunami simulation of the 2011 Tohoku–Oki earthquake. *Journal of Asian Earth Sciences*, *62*, 568-585. (Geology of Baikal Region) doi: 10.1016/j.jseaes.2012.11.007

Vincenty, T. (1975). Direct and inverse solutions of geodesics on the ellipsoid with application of nested equations. *Survey review*, *23*(176), 88–93.

Wang, D., Becker, N. C., Walsh, D., Fryer, G. J., Weinstein, S. A., McCreery, C. S., ... Shiro, B. (2012). Real-time forecasting of the April 11, 2012 Sumatra tsunami. *Geophysical Research Letters*, *39*(19). doi: 10.1029/2012GL053081

Wang, Y., Tsushima, H., Satake, K., & Navarrete, P. (2021). Review on recent progress in near-field tsunami forecasting using offshore tsunami measurements: Source inversion and data assimilation. *Pure and Applied Geophysics*, *178*(12), 5109-5128. doi: 10.1007/s00024-021-02910-z

Wang, Y., Zamora, N., Quiroz, M., Satake, K., & Cienfuegos, R. (2021). Tsunami resonance characterization in japan due to trans-pacific sources: Response on the bay and continental shelf. *Journal of Geophysical Research: Oceans*, *126*(6), e2020JC017037. doi: 10.1029/2020JC017037

Watanabe, Y., Mitobe, Y., Saruwatari, A., Yamada, T., & Niida, Y. (2012). Evolution of the 2011 tohoku earthquake tsunami on the pacific coast of hokkaido. *Coastal Engineering Journal*, *54*(1), 1250002-1-1250002-17. doi: 10.1142/S0578563412500027

Wei, Y., Chamberlin, C., Titov, V. V., Tang, L., & Bernard, E. N. (2013). Modeling of the 2011 Japan Tsunami: Lessons for Near-Field Forecast. *Pure and Applied Geophysics*, *170*(6), 1309–1331. doi: 10.1007/s00024-012-0519-z

Wei, Y., Newman, A. V., Hayes, G. P., Titov, V. V., & Tang, L. (2014). Tsunami forecast by joint inversion of real-time tsunami waveforms and seismic or GPS Data: Application to the Tohoku 2011 Tsunami. *Pure and Applied Geophysics*, *171*(12), 3281-3305. doi: 10.1007/s00024-014-0777-z

Xie, Y., & Meng, L. (2020). A multi-array back-projection approach for tsunami warning. *Geophysical Research Letters*, *47*(14), e2019GL085763. doi: https://doi.org/10.1029/2019GL085763

Yamazaki, Y., Cheung, K. F., & Lay, T. (2013, May). Modeling of the 2011 Tohoku Near-Field Tsunami from Finite-Fault Inversion of Seismic Waves. *Bulletin of the Seismological Society of America*, *103*(2B), 1444–1455. doi: 10.1785/0120120103

Yamazaki, Y., Cheung, K. F., & Lay, T. (2018). A self-consistent fault slip model for the 2011 tohoku earthquake and tsunami. *Journal of Geophysical Research:*

Solid Earth, *123*(2), 1435-1458. doi: 10.1002/2017JB014749

Yokota, Y., Koketsu, K., Fujii, Y., Satake, K., Sakai, S., Shinohara, M., & Kanazawa, T. (2011). Joint inversion of strong motion, teleseismic, geodetic, and tsunami datasets for the rupture process of the 2011 Tohoku earthquake. *Geophysical Research Letters*, *38*(7). doi: https://doi.org/10.1029/2011GL050098

Yoshimoto, M., Watada, S., Fujii, Y., & Satake, K. (2016). Source estimate and tsunami forecast from far-field deep-ocean tsunami waveforms—The 27 February 2010 Mw 8.8 Maule earthquake. *Geophysical Research Letters*, *43*(2), 659-665. doi: 10.1002/2015GL067181

Yun, N. Y., & Hamada, M. (2015). Evacuation behavior and fatality rate during the 2011 Tohoku-Oki earthquake and tsunami. *Earthquake Spectra*, *31*(3), 1237-1265. doi: 10.1193/082013EQS234M

Zhang, Y. J., Witter, R. C., & Priest, G. R. (2011). Tsunami–tide interaction in 1964 Prince William Sound tsunami. *Ocean Modelling*, *40*(3), 246-259. doi: 10.1016/j.ocemod.2011.09.005

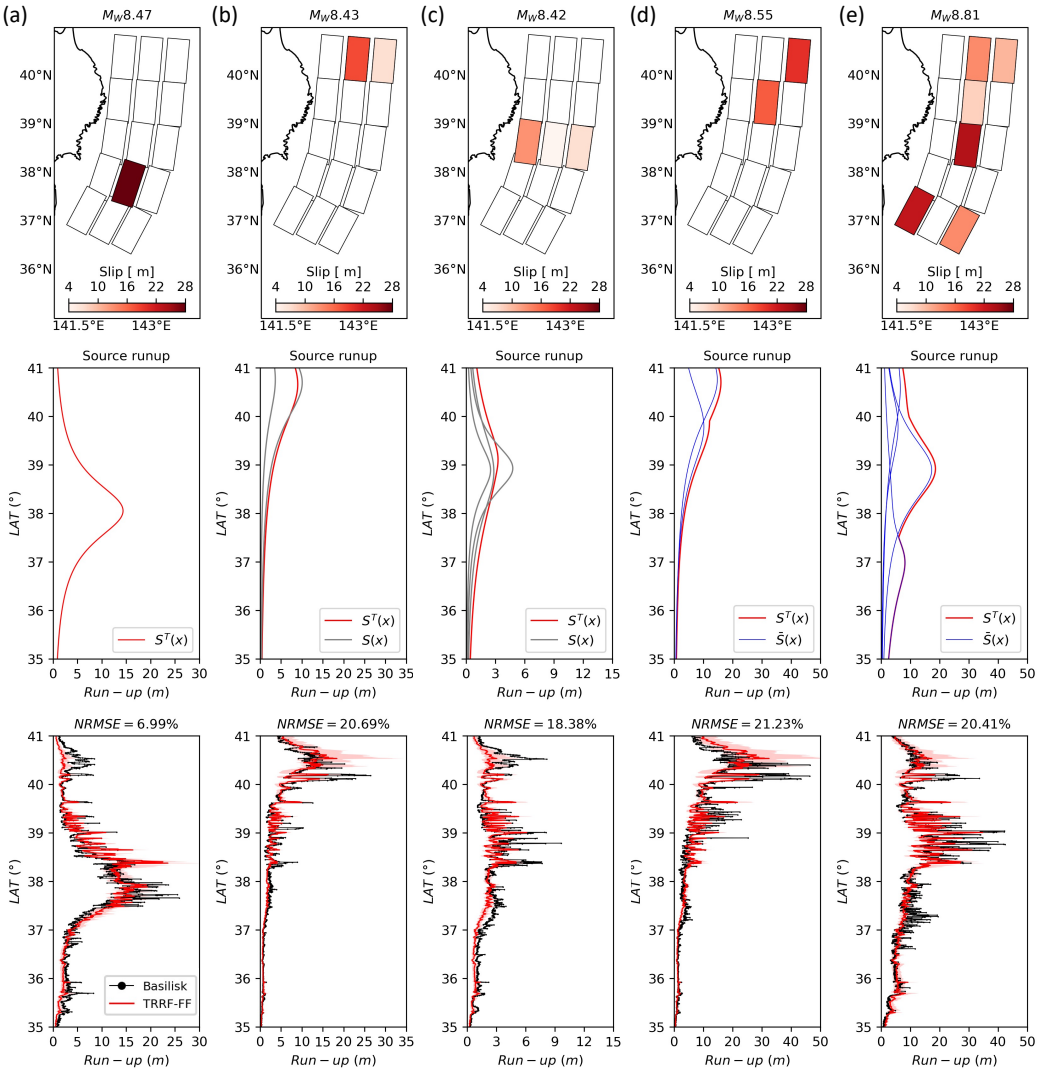

Figure 9. Example results of (a) Test 1, (b) Test 2, (c) Test 3, (d), Test 4, and (e) Test 5. The top panel shows the slip distribution. The middle panel shows the source runup where the gray lines represent the individual source runup $S(x)$, the blue lines represent the combined source runup $\bar{S}(x)$, and the red lines represent the total source runup $S^T(x)$. The bottom panel compares the alongshore tsunami runup distribution between the TRRF-FF model (red line) and the physics-based model Basilisk (black line with circles). The light red represents the range between the 25th and 75th percentiles of the TRRF-FF model prediction.

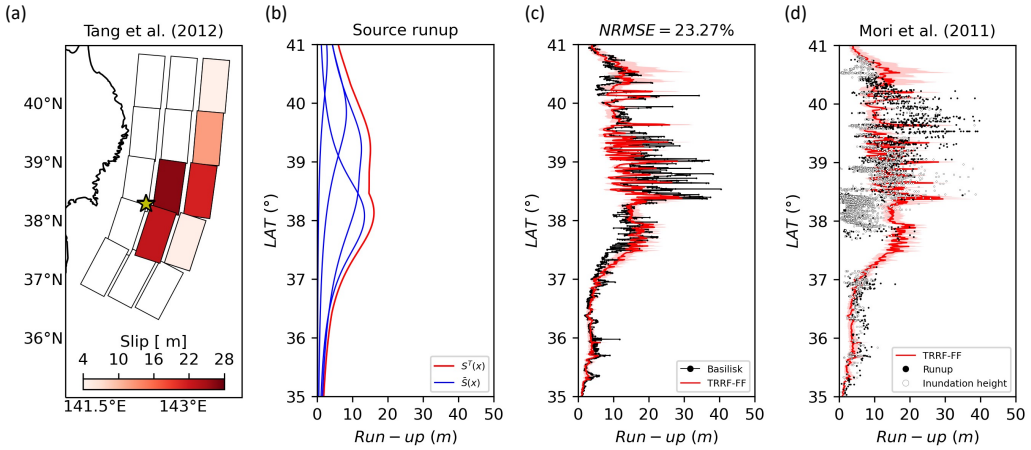

Figure 10. The 2011 Tohoku (Japan) tsunami case results. (a) Slip distribution of Tang et al. (2012). The yellow star represents the USGS epicenter. The fault parameter (dip angle, depth, slip) values of each finite fault can be found in Table 3. (b) The estimated total source runup $S^T(x)$ (red line) and combined source runups $\bar{S}(x)$ (blue lines). (c) A comparison of alongshore tsunami runup distribution between the TRRF-FF model (red) and the physics-based model Basilisk (black line with circles). (d) A comparison between the TRRF-FF model prediction (red) and the tsunami runup (Black circles) and inundation height (white circles) observations of Mori et al. (2011).

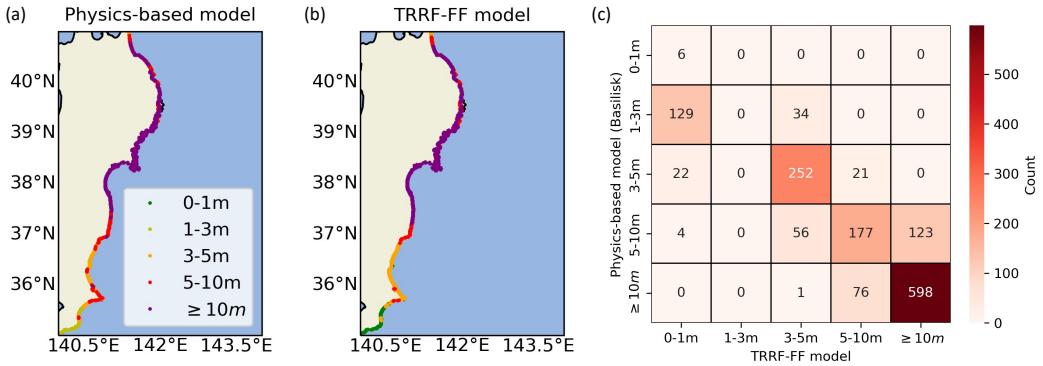

Figure 11. A comparison of tsunami warning levels between (a) the physics-based model Basilisk and (b) the TRRF-FF model. (c) A tsunami warning level confusion matrix.

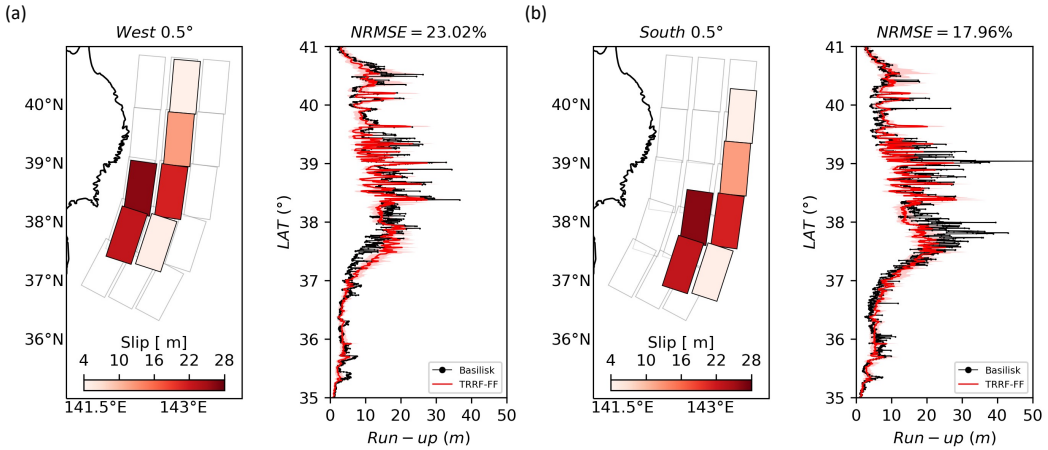

Figure 12. Performance of the TRRF-FF model when Tang et al. (2012)'s slip distribution is shifted by 0.5° (a) to the west and (b) to the south. The left panel represents the slip distribution. The light gray rectangles represent the location of pre-defined tsunami unit sources. The right panel compares the alongshore tsunami runup distribution between the TRRF-FF model (red) and the physics-based model Basilisk (black line with circles).

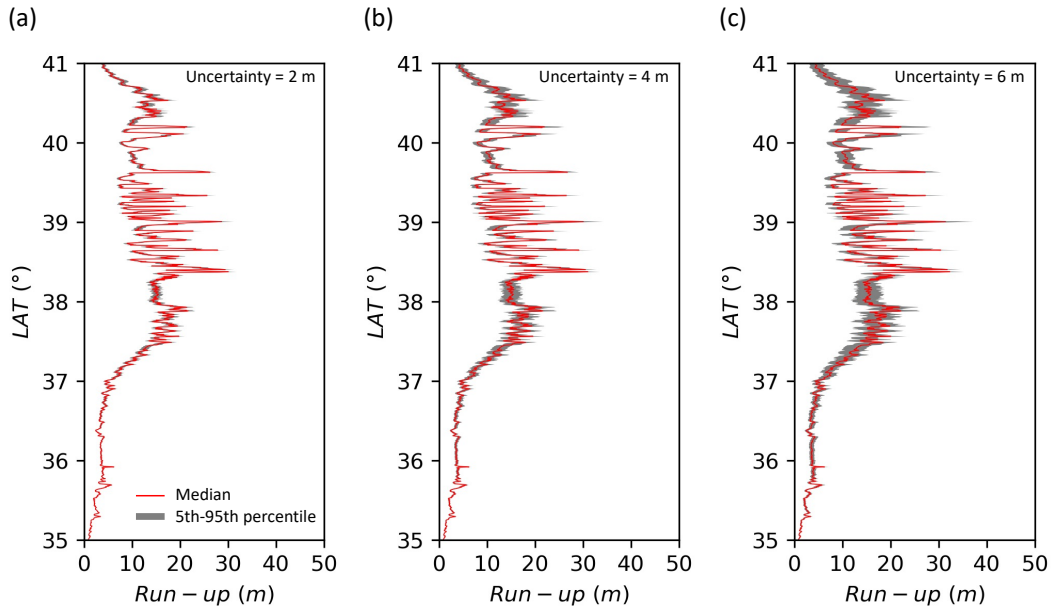

Figure 13. Probabilistic distribution of alongshore tsunami runup when slip uncertainty is (a) 2 m, (b) 4 m, and (c) 6 m. The red line represents the median. The gray represents the 5th-95th percentile.

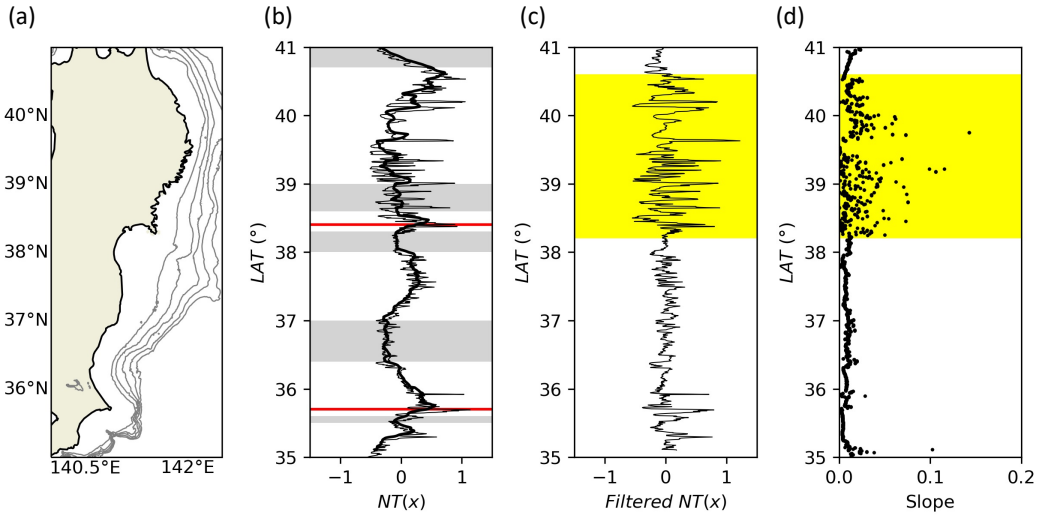

Figure 14. A comparison between the normalized topographic runup and topographic characteristics. (a) Coastline map. The contours (gray lines) are 200 m. (b) Normalized topographic runup $NT^p(x)$ (thin black line) and moving averaged normalized topographic runup (thick black line). The window size of the moving average is 25 data points. The gray areas represent the concave-seaward region. The red lines represent the apex of the peninsulas. (c) Filtered normalized topographic runup (black line), calculated by subtracting the moving averaged normalized topographic runup from the normalized topographic runup. (d) Nearshore slope distribution (black dots) from Athanasiou et al. (2019). Note that nine points between 38.3° and 39.6° and one point at 36.44° where the slope is larger than 0.2 are not plotted for visualization. The yellow areas represent the region where the variation of the filtered normalized topographic runup is larger than that of the other areas.